Rijksuniversiteit Groningen

Master Thesis

Deriving the C/O Ratio in the Outer Regions of PDS-70 Using ProDiMo

Author:
R.P. Ferdinand

Supervisor:
prof. I.E.E. Kamp

Abstract

PDS-70 is a unique case study for planet formation because two young, accreting exoplanets have been directly imaged within. Recent models of the PDS-70 disk do not fully encompass all of the observed gas. In this work, a radial extension ($>$ 120 AU) is made of the gas component of an existing model of PDS-70, with the aim of finding the gas C/O ratio, an important ratio for planet formation, in the disk's outer regions.

Starting from an exponential gas surface density profile, the extension is built by iteratively comparing synthetic $C^{18}O$ (2-1) line emission from ProDiMo to ALMA observations. Similarly, the C_2H (3-2) emission was studied to obtain a C/O ratio for the outer disk gas. In the model, the C/O was increased using carbon addition and oxygen depletion separately.

The shape of the final surface density profile displays a plateau between 120 and 200 AU, where gas density and temperature remain relatively radially constant. Another observation is a higher temperature region within this plateau at z/r = 0.18 which corresponds to a region of depression of CO abundance and a peak in C_3 abundance.

Our model favors a C/O $\gg$ 1, with a C/O of 5 matching observations within 80 AU. This is different from a similar study which found a C/O of 1.01 due to our model containing much less C_2H than theirs. Carbon atoms seem to favor molecules with longer chains (more than two C-atoms). Beyond 80 AU, the C_2H abundance increase is much slower, implying an even higher C/O ratio. An inclusion of non-uniform C/O ratios in the disk model model may be needed to account for this.

Higher C/O ratios were not modeled because the $C^{18}O$ fit is destroyed by raising the C/O to this level. In the future, an inclusion of the C/O ratio as a free parameter in the iterative process is needed to obtain consistent fits for both $C^{18}O$ and C_2H. Future models may also need to vary the dust abundance, as this may also affect the gas emission.

Contents

1 Introduction

The study of planet formation is a relatively young field of research. The first observational evidence of a proto-planetary disk was documented in 1997, when molecular line emissions surrounding the Herbig Ae stars were discovered (Mannings and Sargent, 1997). Understanding disk chemistry has been an active research field since then along with the study of exoplanets.

One of the long term goals of this research field is to find a link between proto-planetary disk chemistry and exoplanet composition. It is intuitive that the chemistry of disks and planets are related, but the link is not an obvious one. As our understanding of disk physics and chemistry grows, we hope to eventually narrow down this gap between disk and planet chemistry and understand how planets form from these disks.

Recent developments, such as the initiation of the Atacama Large Millimeter Array (ALMA), have brought this field of research forward at a pace which is looking very promising, with detailed observations arising in the mm/sub-mm domains, allowing disks to be observed closer to their midplanes because these domains tend to be more optically thin in the outer disk (Rampinelli et al., 2024; Miotello et al., 2022).

PDS-70 is a particularly interesting disk because to date it has some of the most robustly detected young exoplanets, two having been directly imaged within (Keppler et al., 2019; Benisty et al., 2021) and it is therefore a unique case study for planet formation. In this work we model the gas component of the outer regions of PDS-70 with the aim of obtaining the C/O of the gas in these regions. Recent surface density models of this disk encompass a radius of 120 AU from its host star. The dust component is only detected until a distance of 80 AU from the host star (Portilla-Revelo et al., 2021), and can thus not be modeled beyond this radius at this moment. However, line emissions from the gas have been observed up until a radius of 240 AU (Facchini et al., 2021), meaning that current models do not encompass all of the observed flux.

In the remainder of this chapter, an overview is given of the formation and structure of proto-planetary disks and the reader is introduced to the concepts of surface density profiles and C/O ratios and why this ratio is so important for the study of planet formation. Lastly, PDS-70 is introduced as the main focus and the goals and methods of this work are presented.

1.1 Formation and Evolution of Proto-planetary Disks

Proto-planetary (accretion) disks form as a consequence of angular momentum conservation (Williams and Cieza, 2011). The collapse of a molecular pre-stellar core into a star is not just a radial process. there is rotation involved which carries with it angular momentum. To allow the star to continue to contract, this angular momentum must be transported outward. This happens through friction between layers of the disk which are radially separated. Material closer to the star moves faster than material in layers further away from the star. Angular momentum is thus transported to the outer layers of the disk, causing the material closer to the star to lose angular velocity and fall inward (Williams and Cieza, 2011).

Proto-planetary disks are a type of young stellar object (YSO). These objects are categorized through the LADA classifcation, in which YSO's are identified from Class 0 to Class III (see figure 1) depending on their stage in evolution (Greenwood, 2018). This classification is based on the slope of their Spectral Energy Distribution (SED). A Class 0 YSO is a prestellar envelope in which the stellar object is still obscured because of the optical thickness of the envelope. It therefore has little to no optical or near-IR emission. A Class I object is still partially obscured, showing some near-IR emission, but no optical emission. For a Class II YSO, the envelope has become optically thin enough that optical and infrared observation is now possible. They

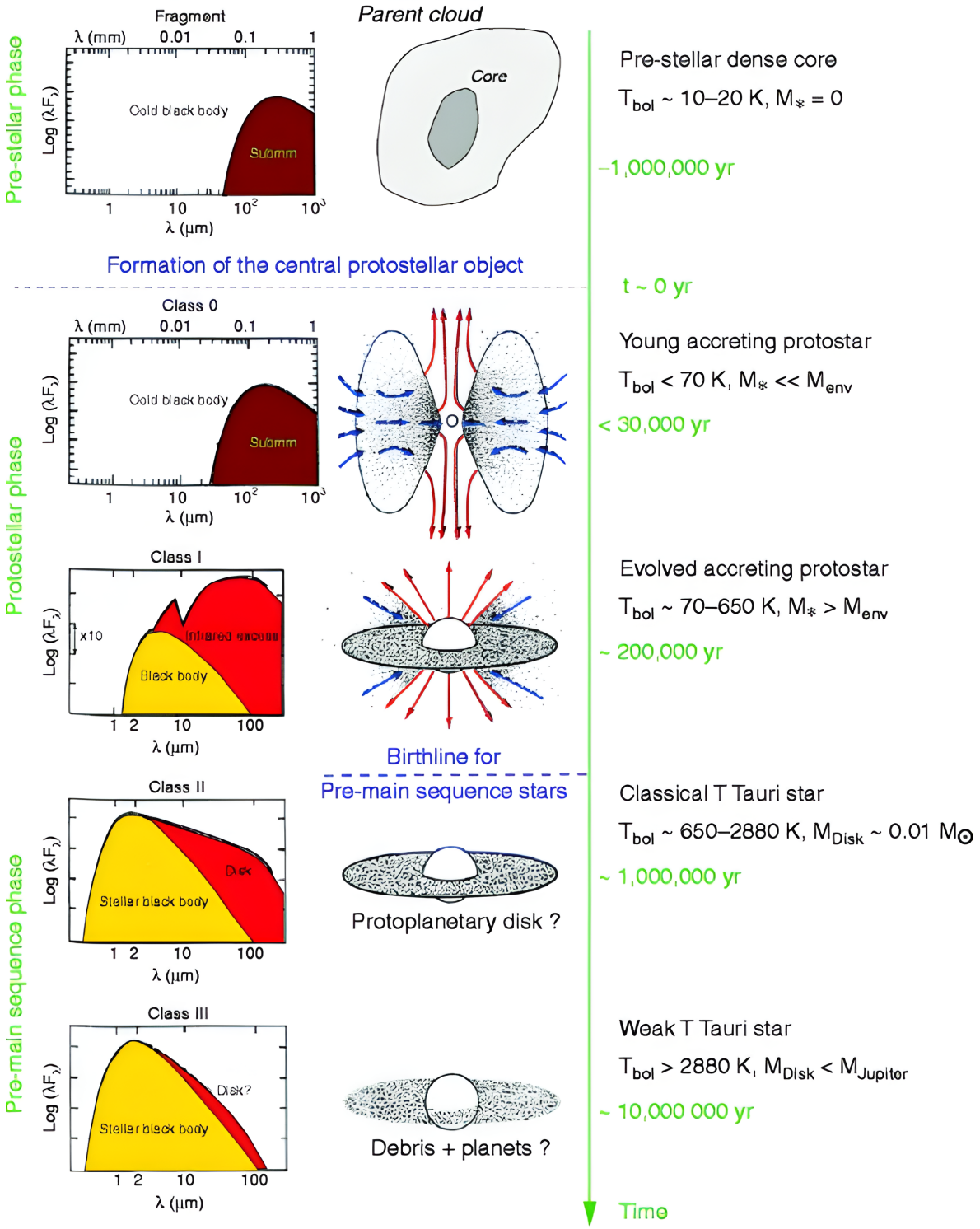

Figure 1: Graphical depiction of the classification of SED's and how they relate to the evolutionary stages of type F-M YSO's, taken from André (2011). A distinction is made between the protostellar phase, in which gravitational free-fall timescales dominate the stellar collapse, and the pre-main sequence phase, in which the stellar accretion is governed by thermal (Kelvin-Helmholtz) timescales. Typical timescales are shown in green. Bolometric temperature and mass properties of the envelope/disk are shown in black.

are also characterized by strong Hα and UV emission. These Class II objects are the classical proto-planetary disk systems. A class-III YSO has lost most of its gas through accretion and photo-dissociation, leaving behind a debris disk containing only dust. Being very weak in the mm regime, The SED will therefore be dominated by the star's own optical and UV emission, and by continuum emission from the dust (André, 2011).

There exists another sub-class of YSO which is in between classes II and III. These disks are called 'transition disks' and are characterized by a gap in the gas density between the star and the beginning of the disk, indicating that the dissipation process has started and the gas is being photo-dissociated away. These disks are particularly interesting to study because the transition from class-II to class-III is still poorly understood (Williams and Cieza, 2011). These transition disks may also hold valuable information about the evolution of these disks and the formation of planets.

1.2 Structure and Observations of Proto-planetary Disks

Each proto-planetary disk has its own unique structure and shape, characterized by the cloud in which it formed, the nature of the core collapse and the stage of planet formation and disk dispersal. Some disks have a large cavity close to the star and therefore resemble rings (see the image of Sz-91 in figure 2). Most disks are likely to form planets through either core-accretion or gravitational instabilities, which also influence the structure of the disk, leaving behind gaps in the dust and the gas structure (see the image of RX-J1852.3-3700 in figure 2) (Williams and Cieza, 2011; Andrews, 2020).

Some disks are asymmetrical, resembling arcs rather than disks. An Extreme case of this type of disk is V1247 Ori (see figure 2, third image from the left), which displays a very high concentration of solid material in a specific region of the system, but almost nothing elsewhere due to extreme dust traps (Andrews, 2020). proto-planetary disks can even display spiral arms in their structure (see for example the image of Elias 27 in figure 2).

Proto-planetary disks have an inclination angle relative to the viewer. Some disks are viewed more face on, while others are viewed more edge on or in between. This is very important to take into account when performing observational analysis of disks. Disks with a larger inclination angle display more rotational motion through Doppler shifts, making it easier to ascertain their motion, whereas face-on disks have a more clearly visible structure due to a lack of obstruction.

While each disk is unique in many aspects, there are also many similarities in their structure and overall composition. This makes it possible to define a standard model of a T-Tauri disk, in

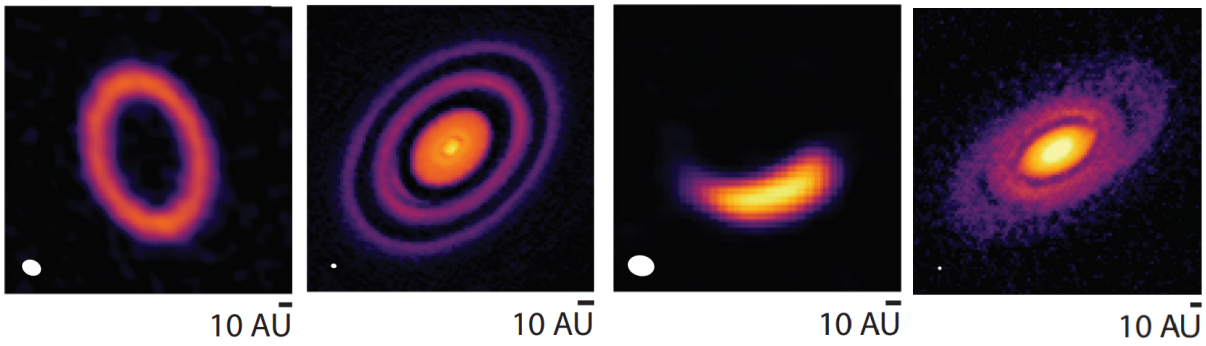

Figure 2: Continuum observation of four disks with different morphologies taken from Andrews (2020). From left to right: Sz-91, RX-J1852.3-3700, V-1247 Ori and Elias 27. The white ellipses in the lower left of each image displays the resolution (beam size) of the image.

which a generic illustration can be made of its structure and particle transport (figure 3), as well as of the location of specific emitting regions (figure 4).

The structure of a typical T-Tauri disk (see figure 3) is characterized by the nature of its physics and (photo)chemistry. As discussed in section 1.1, the function of an accretion disk is to transfer angular momentum away from the star, while transporting material inward. At the same time, these processes cause the material in the disk to interact and elements to react with one another. This can happen through pure gas phase chemistry, but also through gas-dust interactions.

In the upper atmosphere of the disk, the disk material is virtually unshielded from radiation from both the star and interstellar sources (Andrews, 2020). This causes photons to interact with the material more frequently than closer to the midplane, resulting in photochemistry dominating the reactions in this region. This results in overall higher temperatures than further in, where self-shielding prevents the radiation from reaching the material (Williams and Cieza, 2011; Andrews, 2020).

Most of the dust and ices are found close to the midplane of the disk, where they settle because of both gas drag slowing down their rotational motion, and the vertical component of stellar gravity pulling them downwards. The grain size plays an important role in this because

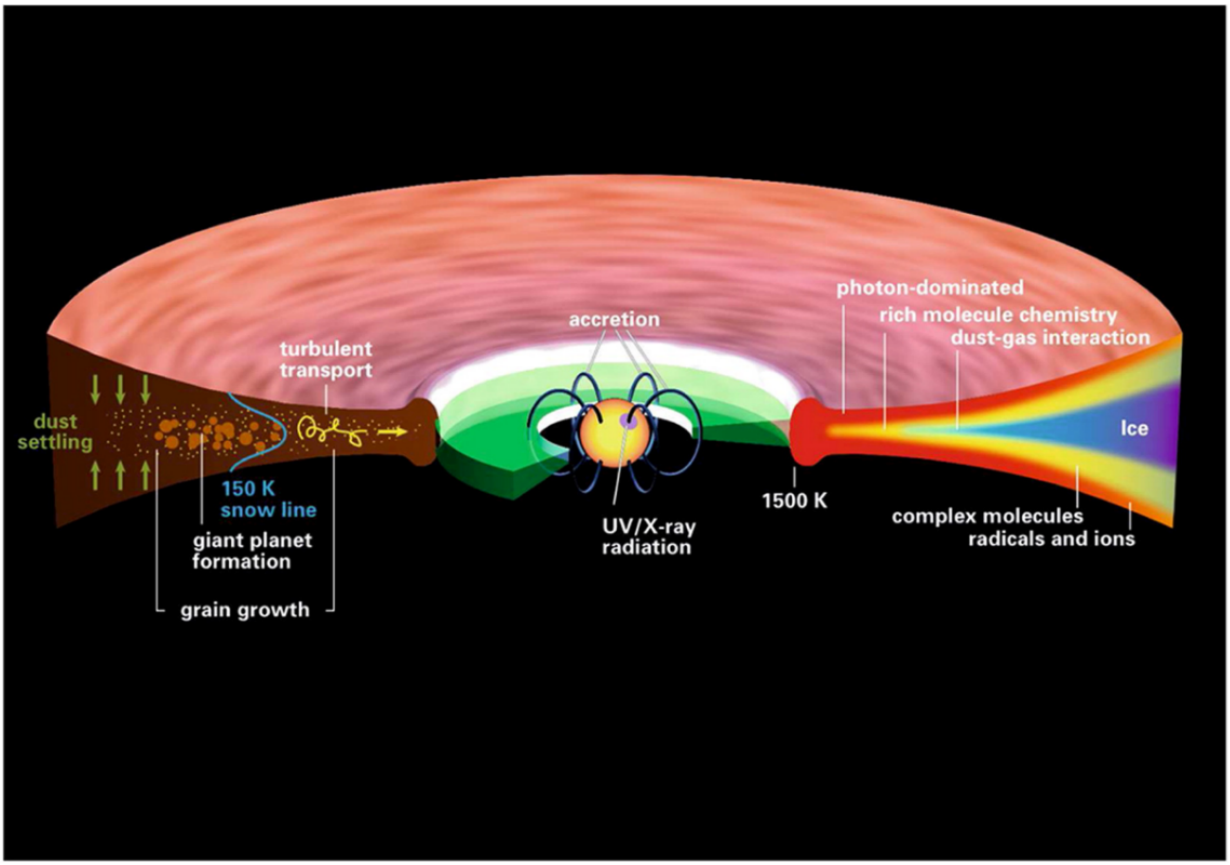

Figure 3: The structure of a typical T-Tauri disk taken from Henning and Semenov (2013) On the left, the physical motion of the dust is illustrated and the H_2O snow line is depicted in blue. On the right, the temperature structure is illustrated as well as the type of chemistry that dominates the region. The thermal zones depicted by the different colors follow the flaring of the disk.

.

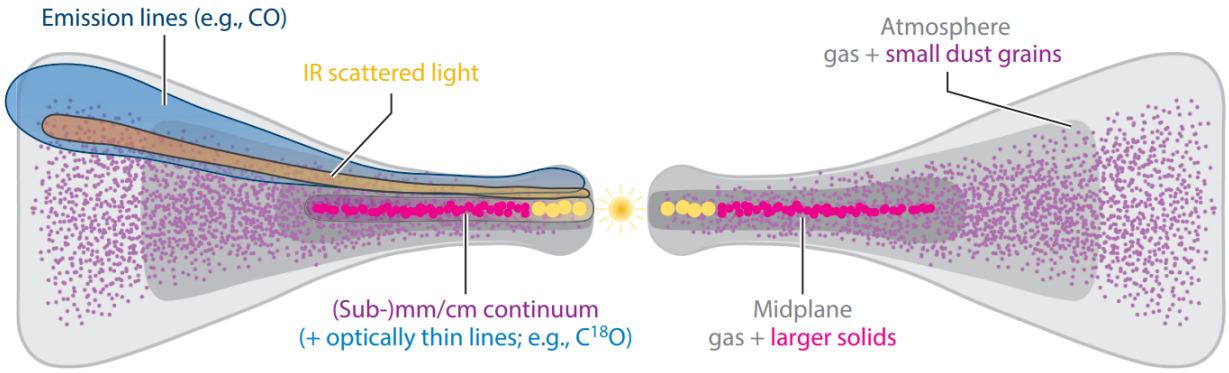

Figure 4: A schematical depiction of the line-emitting regions within a typical T-Tauri disk, taken from Andrews (2020). The gas is depicted by the grey/pink background contours and solids are depicted by the exaggerated sizes and colors. The left side depicts some emission tracers, and the right side defines some structural aspects.

it affects both of these processes. Small grains will feel aerodynamic (Epstein) drag from the gas and is therefore slowed down, while larger grains feel a different (Stokes) drag, which still slows them down but to a lesser extent (Williams and Cieza, 2011). Because larger grains feel less drag from the gas and are also more significantly affected by gravity, they tend to settle faster than smaller grains. This causes them to encounter many smaller dust grains along the way, accelerating the growth process (Williams and Cieza, 2011).

As dust grains collide and grow, their turbulent motion decreases. Because the dust moves faster than the gas it experiences a 'headwind' (the drag mentioned earlier), causing the dust grain to move inward towards the star and also towards the midplane, causing it to accumulate more and more dust (Henning and Semenov, 2013). Once the dust grain becomes large enough, its motion is completely decoupled from the gas and gravity takes over, causing the dust to settle in the midplane even faster. This means that most gas-grain chemistry happens close to the midplane, which also happens to be the region of the disk where the temperatures are generally the lowest. (Williams and Cieza, 2011; Andrews, 2020).

Another important concept for the structure of proto-planetary disks are the snow/ice lines (see figure 3). The ice line of a species is defined as the boundary where the temperature of the disk material is high enough for the species to exist in the gas phase. This creates a condensation front where species freeze out onto grain surfaces (Williams and Cieza, 2011; Henning and Semenov, 2013).

Snow lines were first defined for water. However, more ice lines exist further out. CO has a much lower condensation temperature, and so its ice line is located much further away from the star. Because the temperature structure of a proto-planetary disk is such that the temperature rises with distance from the midplane, the snow line and the other ice lines resemble parabolae (see figure 3).

The origin of the emission follows a pattern which is illustrated by figure 4. Close to the relatively cool midplane, stellar radiation is absorbed by dust and re-emitted (Greenwood, 2018). The dust is therefore visible as sub-mm/cm continuum emission. Line emission from optically thin molecules such as $C^{18}O$ will also be present in this region, their emission being sensitive to the column density of the gas. Further away from the midplane, where temperatures are higher, is where most of the rotational and ro-vibrational line emission from optically thick molecules such as ^{12}CO originates from, as well as IR emission from dust scattering (Greenwood, 2018).

1.3 Gas Surface Density Profiles and C/O Ratios

An important question in the research of star and planet formation is how disk chemistry relates to the composition of exoplanets. The link between these is not yet very clear (Müller et al., 2018). However, we do know that the surface density profile and the carbon to oxygen (C/O) ratio of a proto-planetary disk play a very important role (Eistrup et al., 2018). This is true for both the gas and the dust component of the disk.

The surface density profile of a proto-planetary disk illustrates its basic radial structure. It tells you how much material is distributed per unit surface area as a function of radius in the disk (see figure 5 for an example). Dust and gas are distributed differently (see chapter 1.2) and therefore have separate surface density profiles. How the gas and dust profiles differ is quantified by the gas-to-dust ratio Δ_{gtd}. This can vary significantly throughout the disk as a result of planet formation or dust traps. It is also affected by properties of the dust itself, such as the grain size.

The surface density profile is important for planet formation because it regionally indicates

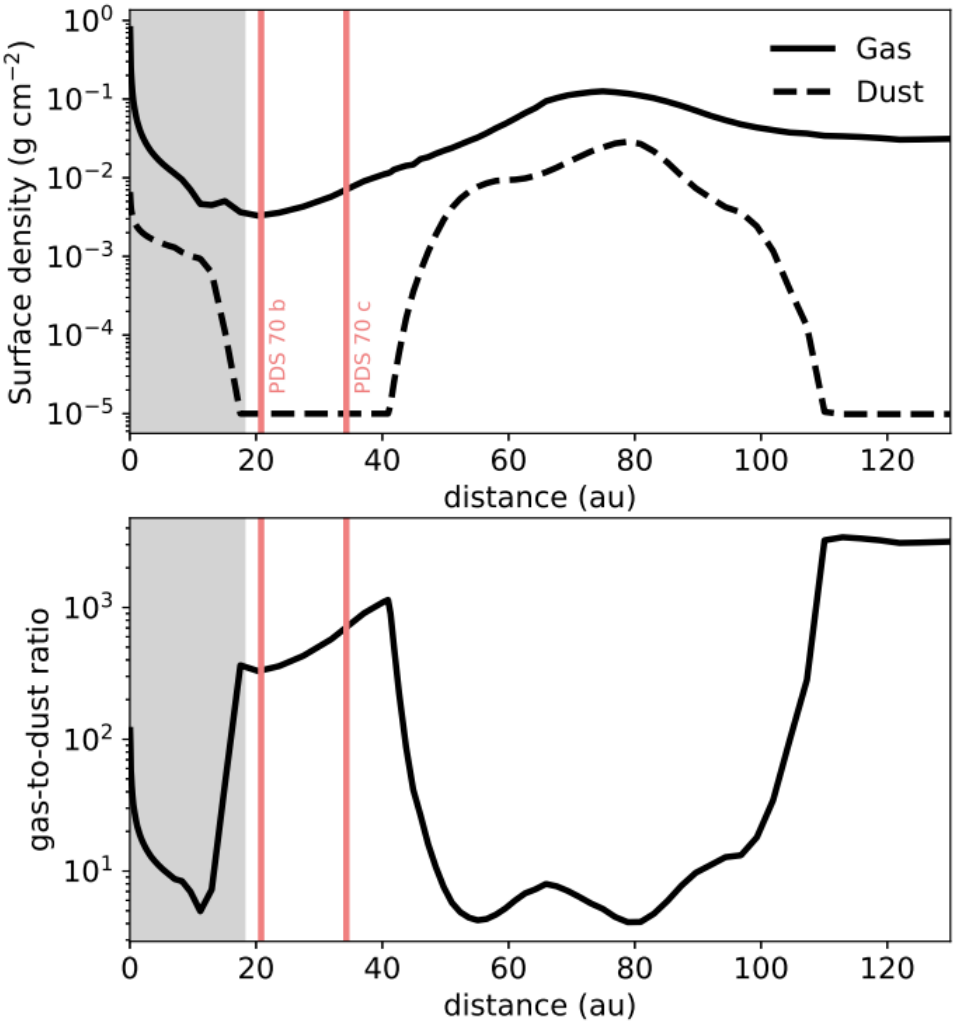

Figure 5: Top: surface density of the proto-planetary disk PDS-70 as a function of distance from the central star. Bottom: gas-to-dust ratio of the same disk as a function of the same distance. taken from Portilla-Revelo et al. (2023).

the abundance of available material in the disk. Because the formation of a planet consumes material from the disk, a gap can form (depending on the planetary mass) and therefore a sudden drop is expected in the surface density of both the gas and the dust. Figure 5 illustrates this. The visible gap in the gas and dust profiles from ~ 20 to ~ 50 AU is caused by the formation of two exoplanets in this system. The dust is affected more significantly than the gas, as the gas-to-dust ratio becomes larger in the gap.

In order to determine the gas surface density profile of a disk one needs to trace it with molecules that follow the distribution of the total gas closely. CO is such a molecule because it traces H_2 which is what the bulk of the gas consists of. Furthermore, it is important that the molecule being traced is optically thin so that its flux traces the column density and not the temperature. (Portilla-Revelo et al., 2021). Therefore, the optically thin $C^{18}O$ isotopologue is an ideal choice.

The C/O ratio determines in large part the abundance of molecules expected to find in a proto-planetary disk. In a carbon-rich disk one expects the chemistry to be carbon-dominated, with molecules such as C_2H_2, C_2H and HCN being very abundant (Eistrup et al., 2018; Cridland et al., 2023). However, for oxygen dominated disks, the expected chemistry favors oxygen rich molecules such as H_2O and OH groups (Eistrup et al., 2018).

The C/O ratio is the most popular ratio for tracing planet formation because of several reasons which are described in Cridland et al. (2023). Carbon and oxygen containing molecules are among the most abundant species in the universe and are easy to observe in the near- to mid-IR. C-species also have very different condensation temperatures from O-species, which creates a clear gradient in the C/O ratio throughout the disk for both the dust and the gas. This allows different formation models to predict chemical differences in gas-giant atmospheres based on the starting location of their formation (Cridland et al., 2023).

The relation between proto-planetary disk chemistry and exoplanet compositions is very complicated and non-linear. Processes such as planet migration and disk material motion can change the composition of forming bodies greatly and therefore add more degrees of freedom (Cridland et al., 2023), making it difficult to directly connect planetary composition to disk chemistry.

Realistically, a proto-planetary disk does not have a single C/O ratio (Cridland et al., 2023). Much like the surface density profile, it is a value which varies throughout the disk radially and vertically. Ice lines also affect the C/O ratio, as freeze-out of material onto dust grains alters the abundance of carbon-rich and oxygen-rich molecules within both the gas and the dust.

1.4 Introducing PDS-70 and the Goal of This Work

This work focuses on PDS-70, a T-Tauri star located in the Centaurus constellation. The proto-planetary disk around this star is a transition disk and has recently been subject to a lot of attention in the field of star and planet formation (Cridland et al., 2023; Facchini et al., 2021; Portilla-Revelo et al., 2021, 2023; Rampinelli et al., 2024). The star is located 113.47 Pc away from Earth and its mass and radius are approximately 0.76 $M_\odot$ and 1.26 $R_\odot$ respectively (Rampinelli et al., 2024; Portilla-Revelo et al., 2023). Its bolometric luminosity is 0.35 $L_\odot$ (Portilla-Revelo et al., 2023). The disk surrounding it has an inclination of 51.7° and a position angle (PA) of 160.4° (Portilla-Revelo et al., 2023).

PDS-70 was surveyed in 1992 as a part of the Pico dos Dias survey, which made use of IRAS satellite measurements to identify pre-main sequence stars by analyzing their photometry (Sartori et al., 2009). A little over a decade later, its proto-planetary disk was imaged by the use of the phase-mask coronagraph on the VLT (Riaud et al., 2006).

What makes this planetary system stand out so much is the fact that two forming exoplanets have been directly imaged within (see figure 6). In 2018, VLT/Sphere observations indicated that

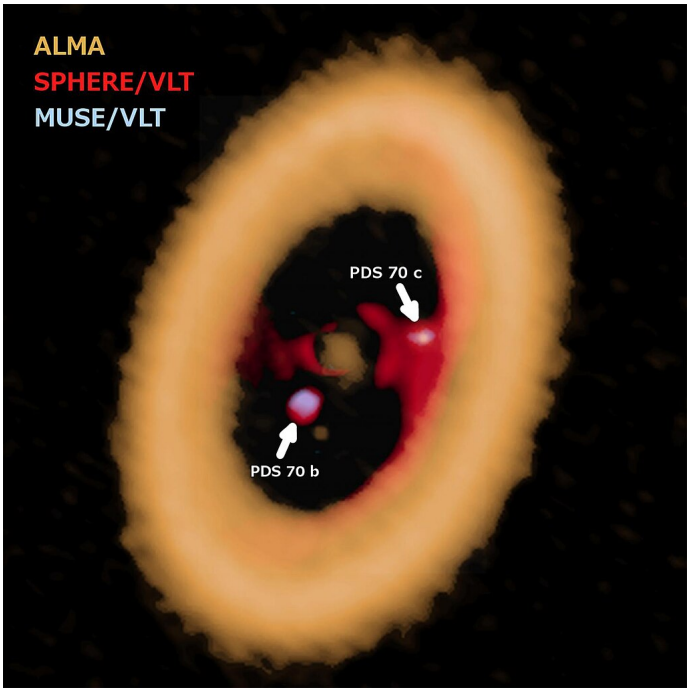

Figure 6: Image of the 855 μm continuum emission of the PDS-70 system. The image is obtained from combining ALMA and VLT data. The planetary companions PDS-70b and PDS-70c are indicated with the arrows. Image credit: ALMA (ESO/NAOJ/NRAO) A. Isella; ESO. Taken from Liu and Ji (2020).

PDS-70 had indeed a companion which was subsequently dubbed PDS-70b (Müller et al., 2018). One year later, further observations confirmed the existence of a second companion, PDS-70c (Mesa et al., 2019).

The two planets in question are sizable gas giants, PDS-70b and -c having maximum masses of 4.9 M_{jup} and 13.6 M_{jup} respectively (Portilla-Revelo et al., 2021). Dust models show that the location of these planets ($\sim$ 20.7 AU and $\sim$ 33.9 AU respectively (Portilla-Revelo et al., 2021)) are in line with gaps in the gas and dust surface density profiles of the proto-planetary disk, confirming that the planets accrete material from the disk.

Models have been developed to study PDS-70's disk chemical composition (Portilla-Revelo et al., 2021, 2023; Cridland et al., 2023). These models encompass a radius of $\sim$ 120 AU, covering the detected dust emission, which reaches to $\sim$ 80 AU. These models do not yet encompass the full extent of the detected gas line emissions, which reach out towards $\sim$ 240 AU. The goal of this work is to extend this model for the gas in PDS-70 and obtain its surface density profile and C/O ratio. Using the ProDiMo code (see section 2.2), the disk structure and chemistry is modeled, as well as synthetic observations of CO (2-1) line emission. These (particularly those of the optically thin $C^{18}O$ isotopologue) are compared to observations from ALMA in order to obtain a gas surface density profile that fits the observation.

To obtain a C/O ratio for the PDS-70 gas, synthetic C_2H (3-2) line emission is compared to observation. The C/O ratio is varied in two ways: by decreasing oxygen abundance and by increasing carbon abundance. The study in (Cridland et al., 2023), in which the C/O ratio of PDS-70 is studied in a similar way, was used as a point of reference and comparison to study differences between the two models.

2 Comparing ALMA Observations to ProDiMo Models

In this chapter I will go over the general methodology of this work. I will describe the observation data that was used as well as the structure of the ProDiMo code and how the input surface density structure is converted to synthetic images. In the last section of this chapter, I will explain the post-processing steps which these synthetic images were put through (CASA and GoFish) in order to compare them to observations.

2.1 ALMA Observations of PDS-70

The Atacama Large Millimeter Array is an ideal instrument for observing gas in proto-planetary disks, because it is equipped to detect the rotational emission which is typical for this component. It is a large array of 66 antennae all linked together as an interferometer.

Observations of PDS-70 relevant to this work are those of the ALMA program # 2019.1..01619.S (Rampinelli et al., 2024; Law et al., 2024; Facchini et al., 2021). The observations are shown in the form of channel maps imaging the flux of specific line transitions (see figure 7).

Because of the Doppler Effect caused by the disk's rotation, a molecule's emission frequency varies throughout the disk. On the side of the disk which is moving away from the observer the frequency is slightly red-shifted. Conversely, the part which is moving towards the observer is blue-shifted. The line flux is therefore observed in each of these frequencies individually as a function of velocity. A single image of the total line flux in the disk can be obtained by integrating all the channels over the velocity axis, which results in a moment-zero map. I will explain this in more detail in chapter 2.3.

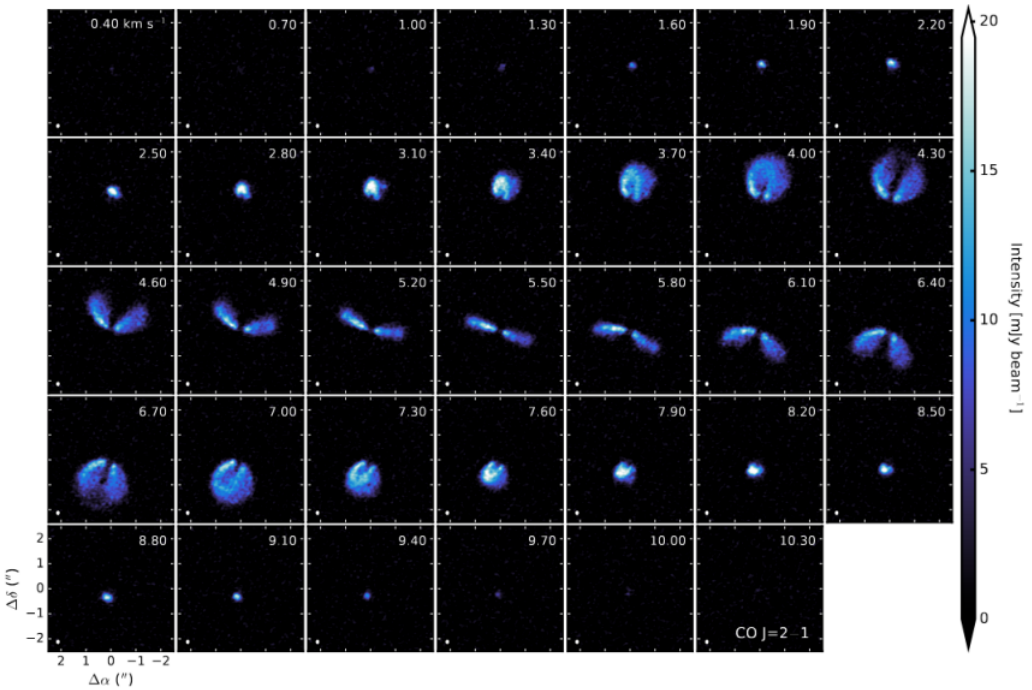

Figure 7: ALMA observation channel maps showing the intensity of the 2-1 transition of ^{12}CO taken from Law et al. (2024) as a function of velocity (km s^{-1}). Displayed is also the size of the beam in the lower left corner of each image. Each channel map shows the line flux in a different part of the disk, going from the top right corner, through the middle, to the bottom left.

2.2 The ProDiMo Code

ProDiMo stands for Proto-planetary Disk Model. This code, which has been developed over the last two decades (Woitke et al., 2009), calculates the density structure of the gas and dust components of a disk given a semi-analytic model in which basic disk properties (e.g. disk radius, vertical height, flaring angle, stellar parameters, etc.) are already defined. Disk chemistry is modeled given a chemical network and a selection of species by choice. Rate coefficients are obtained from the UMIST-2012 database (McElroy et al., 2013). With the use of Ray Tracing, ProDiMo can also generate synthetic line observations in the form of channel maps (see figure 9).

In this section, I will go over the overall structure of the code and briefly outline the steps as they are implemented in this work. For more intricate details about the parametrized structure, see Woitke et al. (2016). For the chemical network and rates, see Kamp et al. (2017).

2.2.1 Overall structure of the Code

Figure 8 illustrates the basic steps of the ProDiMo code as it was used in this work. For the parametrized density structure, ProDiMo requires a semi-analytic model of the gas and the dust

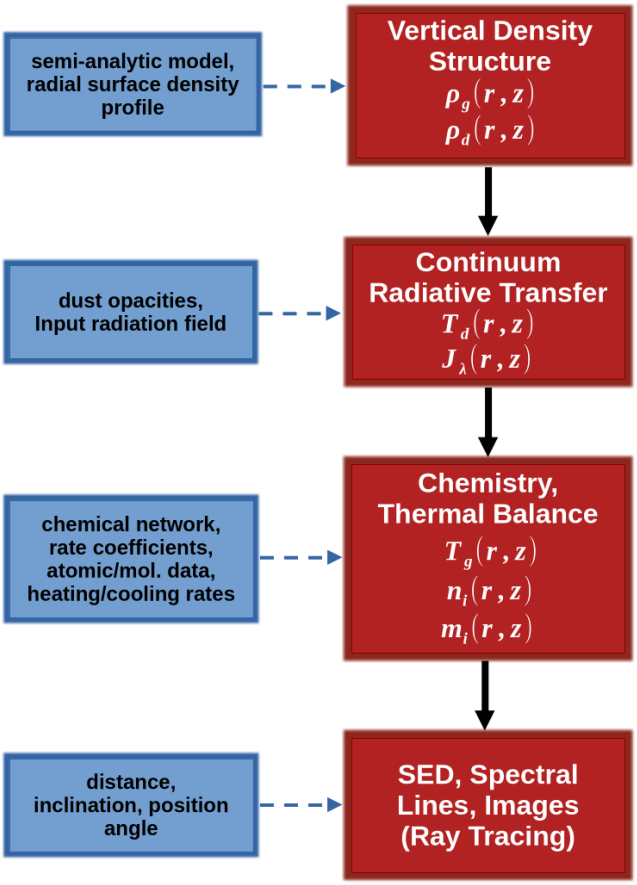

Figure 8: Flow chart showing the general steps of the ProDiMo code with the variables that are calculated (red boxes) and the input that is required for each step (blue boxes)

in a disk. The radius and vertical height of the disk are divided in grid points. In this work, 152 radial- and 100 vertical grid points were used. In our case, The model was set up using a radial column density profile.

2.2.2 Vertical Density Structure

In this work, the vertical gas density structure was parametrized in a similar way as in the MCFOST algorithm (Pinte et al., 2009), where a Gaussian vertical density structure is assumed, in which, for each grid point, the gas density is derived:

$$\rho_g(r,z) = \frac{\Sigma_g(r)}{\sqrt{2\pi} * h(r)} \exp\left(-\frac{z^2}{2h(r)^2}\right) \left[\mathrm{g} * \mathrm{cm}^{-3}\right] \tag{1}$$

Here, $\Sigma_g(r)$ is the radial surface density of the gas and $h(r)$ is the gas scale height, which is calculated with the following equation:

$$h(r) = h_0 \left(\frac{r}{r_0}\right)^{\beta} \tag{2}$$

Here, h_0 is the reference scale height at reference radius r_0 and β is the disk flaring exponent. For this work, the same values were used as in Portilla-Revelo et al. (2023): $h_0 = 10.60$ AU, $r_0 = 100$ AU, and $\beta = 1.14$.

The dust density $\rho_d(r,z,a)$ was calculated by assuming that the dust surface density is proportional to the gas surface density, with the gas-to-dust mass ratio Δ_{gtd} (dependent on grain size a) as proportionality factor:

$$\Sigma_d(a) = \frac{\Sigma_g}{\Delta_{gtd}(a)} \tag{3}$$

Dust settling is also taken into account according to Dubrulle et al. (1995), in which the upward turbulent mixing and the downward gravitational settling are assumed to be in equilibrium (Woitke et al., 2016).

2.2.3 Continuum Radiative Transfer

In the continuum radiative transfer step (Woitke et al., 2016; Oberg et al., 2022), the internal radiation field $J_\lambda(r,z)$ is derived by solving the radiative transfer equation. This step requires knowledge of the optical constants for the dust:

$$\frac{1}{\rho_d(r,z)} \frac{\partial I_\nu(r,z,\hat{k})}{\partial s} = -\kappa_\nu^{\mathrm{ext}} I_\nu(r,z,\hat{k}) + \kappa_\nu^{\mathrm{abs}} B_\nu(T_d) + \kappa_\nu^{\mathrm{sca}} J_\nu(r,z) \tag{4}$$

Here, I_ν is the spectral intensity, B_ν is the Planck function, and k_ν^{ext} k_ν^{abs} and k_ν^{sca} are respectively the extinction, absorption and scattering coefficients of the dust.

The equation is solved according to the ray tracing method described in Pinte (2015), where rays are traced along several propagation pathways. This is done iteratively for each grid point until convergence is reached for the radiation field, or until the maximum number of ray iterations has been reached. In this work, this maximum was set to 100 rays.

The dust temperature is derived by assuming radiative equilibrium, meaning that all the radiation that the dust absorbs is also re-emitted. The dust temperature is then derived with the radiative equilibrium equation:

$$\int_0^\infty \kappa_\nu^{\rm abs} B_\nu(T_d(r,z))d\nu = \int_0^\infty \kappa_\nu^{\rm abs} J_\nu\,(r,z)\,d\nu \tag{5}$$

2.2.4 Chemistry and Thermal Balance

For the chemistry step (see also Kamp et al. (2017)) species densities (here n_i) are derived for each molecule by solving the rate equation which describes the production and destruction of chemical species:

$$\frac{dn_i}{dt} = \sum_{jkl} R_{jk\to il}(T_g) n_j n_k + \sum_{jl}(R^{ph}_{j\to il} + R^{cr}_{j\to il}) n_j$$
$$-n_i \left(\sum_{jkl} R_{il\to jk} n_l + \sum \left(R^{ph}_{i\to jk} + R^{cr}_{i\to jk} \right) \right) \tag{6}$$

Here $R_{jk\to il}$ is a rate coefficient for two gas phase reactants j and k forming the products i and l. $R^{ph}_{j\to il}$ is a photochemistry reaction and $R^{cr}_{j\to il}$ is a cosmic ray reaction. The rate coefficients were obtained from the UMIST-2012 database (McElroy et al., 2013). In our case, $\frac{dn_i}{dt} = 0$ because we assume steady state conditions.

In order for ProDiMo to solve this equation, it requires a chemical network which is based on a selection of atomic elements and molecular species connected through a series of reactions. It also requires atomic and molecular data, such as adsorption energies, which were obtained from Aikawa et al. (1996). In our case, the large chemical network from Kamp et al. (2017) was used, which includes longer chain hydrocarbons (molecules with more than two carbon atoms). The hydrocarbons were allowed to have chains of up to four carbon atoms. This is important for the C/O ratio (see chapter 5). Also important to note is that no isotope specific reactions are included in the network, nor is isotope selective photodissociation (Kamp et al., 2017). The isotope ratios are assumed to be constant for each element. In this work, isotopic ratios of the local ISM are assumed. More specifically for carbon and oxygen: $[^{12}\mathrm{C}]/[^{13}\mathrm{C}] = 77$, and $[^{16}\mathrm{O}]/[^{18}\mathrm{O}] = 560$ (Portilla-Revelo et al., 2023).

The gas temperature (T_g) is obtained by balancing the heating and cooling rates. Several heating and cooling processes are taken into account, such as viscous heating, X-ray heating, atomic/molecular line cooling and collisional heating and cooling. For this, a non-LTE escape probability method is used, described in Woitke (2015), in which thermal energies are derived for N-level heating and cooling which yields the gas temperature.

Because the reaction rate coefficients are dependent on the gas temperature (see equation 6) this new gas temperature leads to a change in the species densities and the level populations of each species. This in turn changes the amount of cooling radiation from each species, which changes the gas temperature once again. As a consequence, the chemistry and the gas temperature derivation are coupled, and also therefore iteratively solved until convergence is reached for both.

2.2.5 Generating Synthetic Image Data

As a final step, ProDiMo again uses ray tracing to generate synthetic SED's and image data in the form of channel maps as a function of velocity through the calculation of line radiative transfer (see figure 9). This time, instead of tracing the rays in random propagation directions, the tracing is done in only one direction between the observer and the object.

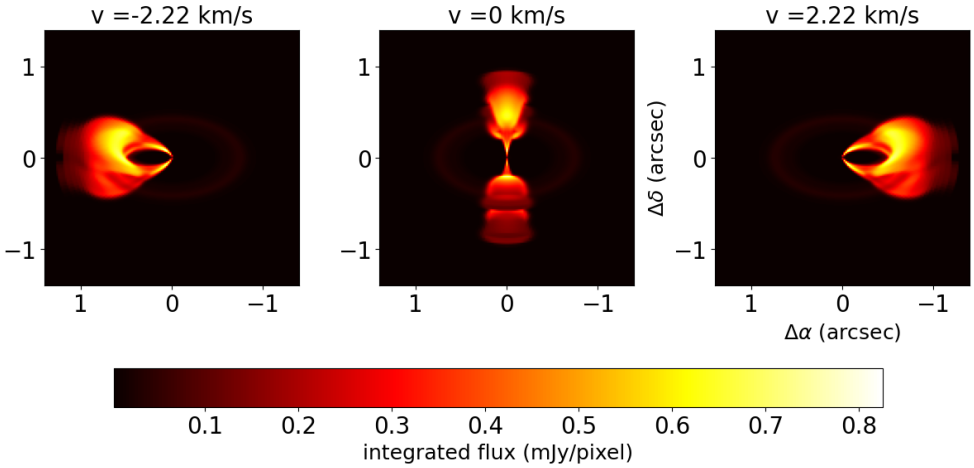

Figure 9: An example set of simulated channel maps of the ^{12}CO (2-1) line of PDS-70 as they are produced in ProDiMo, using the model parameters from Portilla-Revelo et al. (2023) as input. Note that the total data cube was much larger. The total number of channels in the simulated cubes was set to 91. This figure shows just three of them for illustration.

This step requires specifications of the basic properties of the disk, such as distance from Earth (113 Pc) and disk inclination (51.7°). It also requires specification of the line transitions to be traced. In our case, the lines that were traced were the 2-1 transitions of three CO isotopologues and the 3-2 transition of C_2H, which was divided into two fine structure components which were co-added later (see also table 1).

This step also requires specification of the image dimensions. The pixel scale defines the resolution of the image and is specified in terms of a two-dimensional grid, specifying the number of pixels on the sides of the image, and the outer radius from the center of the image in AU. Note that this outer radius does not have to be the same radius as in the model structure. It is a separate value just used for the line images and does not affect the structure of the model itself. In our case, the image was 201 by 201 pixels, covering a radius of 340 AU.

2.3 Comparing Simulation to Observation using CASA and GoFish

In order to compare the synthetic channel maps to real data, one also has to make sure that the synthetic images match the observations. One wants the synthetic images to seem like they were observed with the same instrument configuration as the real data (same resolution and orientation), and also that they both underwent the same post-processing. For this, we use the CASA package version 6.6.0. (McMullin et al., 2007), a library of functions which are used for the reduction of radio-astronomical data.

If we compare the raw ProDiMo simulations of the ^{12}CO (2-1) line from figure 9 to the real observations from figure 7, several striking differences can be seen. Firstly, the disk in the simulated data is oriented such that the semi-major axis aligns with the right ascension offset ($\Delta\alpha$) and the semi minor axis is aligned with the declination offset ($\Delta\delta$). This is not the case for the real observations, which show a counterclockwise position angle of 70.4°.

Secondly, in real data, the resolution of the image is determined by the size of the observed beam and not by the pixel scale like in the synthetic images. Therefore, to emulate the observations of figure 7, the simulated channel maps were convolved to the elliptical beam of the real observations. Each line transition has its own resolution and position angle (Do not confuse this

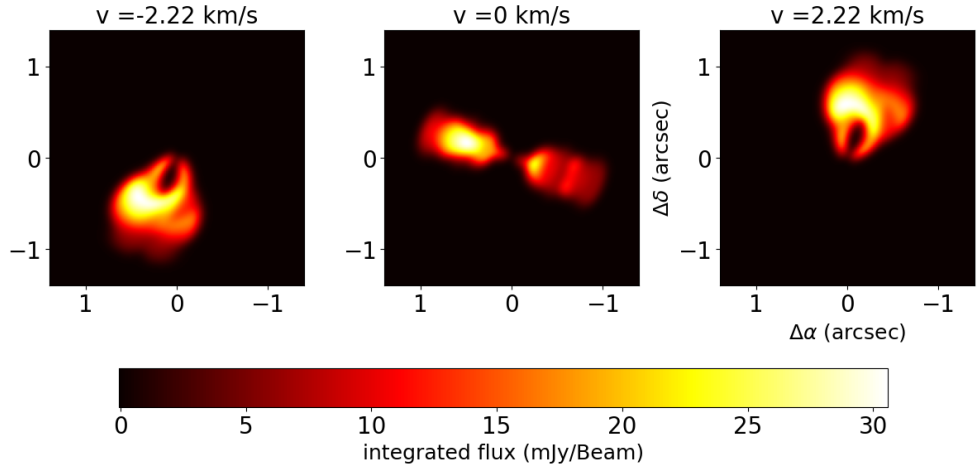

Figure 10: The same simulated ^{12}CO channel maps as figure 9, but rotated, convolved and continuum-subtracted to match the observations of figure 7, with the use of the CASA package (McMullin et al., 2007).

with the PA of the disk). These, along with the rest frequency of each transition, are displayed in table 1.

The last difference is that in the simulated data, continuum emission can be seen throughout all the channels. This needs to be subtracted in order for the image to display line flux only. This continuum subtraction is also done for the real observations and is therefore necessary in our synthetic images.

It is important to do the post-processing in the correct order. First, the image was rotated

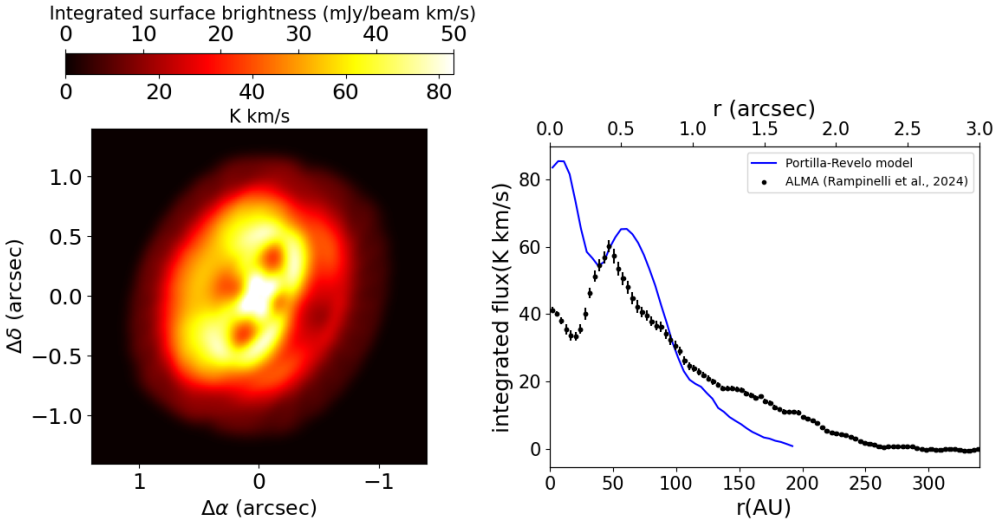

Figure 11: **Left**: Moment-0 map of the simulated ^{12}CO emission (Portilla-Revelo model) obtained by integrating all the channel maps over the velocity axis. It is displayed in both units of integrated surface brightness (mJy/Beam km/s) and brightness temperature (K km/s). The brightness temperature unit was obtained using the Rayleigh-Jeans approximation. **Right**: The corresponding azimuthally averaged radial profile in units of brightness temperature, compared to observation from Rampinelli et al. (2024).

using the 'rotate' task within the CASA package. After rotation, the 'convolve2d' task was implemented in which a gaussian beam was used as input for the beam size. Then, the 'imcontsub' task was used to subtract the continuum flux from each channel map in the cube. It was assumed that about a third of the channel maps were free of lines and thus contained only continuum emission. Figure 10 displays some of the ^{12}CO synthetic channel maps after completion of these operations.

In order to get the total surface brightness of a line in the disk, the CASA package was used once again to integrate the line flux I_v over the velocity axis dv to obtain a moment-zero (M_0) map (see also figure 11):

$$M_0 = \int I_v dv$$

In a last step, radial profiles of the line flux were extracted. Using the GoFish package (Teague et al., 2018), the moment-zero maps were azimuthally averaged. These radial profiles were then compared directly to those of Law et al. (2024) for C^{18}O and to those of Rampinelli et al. (2024) for ^{12}CO, ^{13}CO and C_2H.

Further inspection of the ProDiMo models was done with the use of the python package prodimopy. Information such as the temperature structure, gas density and molecular abundances in the gas and ices were inspected to study how and why they change with the surface density and the C/O ratio.

Transition	**Rest Frequency** (GHz)	**Beam** (θ_{maj} x θ_{min} (PA))
^{12}CO (2 - 1)	230.5380	0.133" x 0.104" (96.67°)
^{13}CO (2 - 1)	220.3986	0.155" x 0.124" (100.01°)
C^{18}O (2 - 1)	219,5603	0.160" x 0.130" (−82.40°)
C_2H ($3_{7/2,4}$ - $2_{5/2,3}$)	262.0042	0.203" x 0.151" (95.57°)
C_2H ($3_{7/2,3}$ - $2_{5/2,2}$)	262.0064	0.203" x 0.151" (95.57°)

Table 1: Properties of the line transitions as used in this work. Beam size values were set to emulate the observations of Rampinelli et al. (2024) for ^{12}CO,^{13}CO and C_2H and of Law et al. (2024) for C^{18}O.

3 Obtaining the Gas Surface Density Profile

To obtain the gas C/O ratio in PDS-70's outer disk, the density structure of the disk gas was modeled first. This was done in an iterative procedure where synthetic $C^{18}O$ (2-1) line observations were compared to observation from Law et al. (2024), starting from an exponential first guess model. The ^{12}CO (2-1) and ^{13}CO (2-1) lines were also modeled and visually compared to data from Rampinelli et al. (2024), but were not used in the iterative procedure. In the remainder of this chapter I will present and explore the first guess model, introduce the iterative procedure, and present the final model, exploring the changes that arise in its structure compared to the first guess model.

3.1 The Initial Model

To get started on an extension for the Portilla-Revelo model, an exponential function taken from (Cridland et al., 2023) (hereafter referred to as 'iteration zero') is used as a first guess (see also figure 12):

$$\Sigma_{gas} = \Sigma_c \left(\frac{R}{R_c}\right)^{-\gamma} \exp\left(-\left(\frac{R}{R_c}\right)^{2-\gamma}\right) \tag{7}$$

Here, R_c is the critical (tapering off) radius which we took to be about 40 AU for PDS-70, Σ_c is

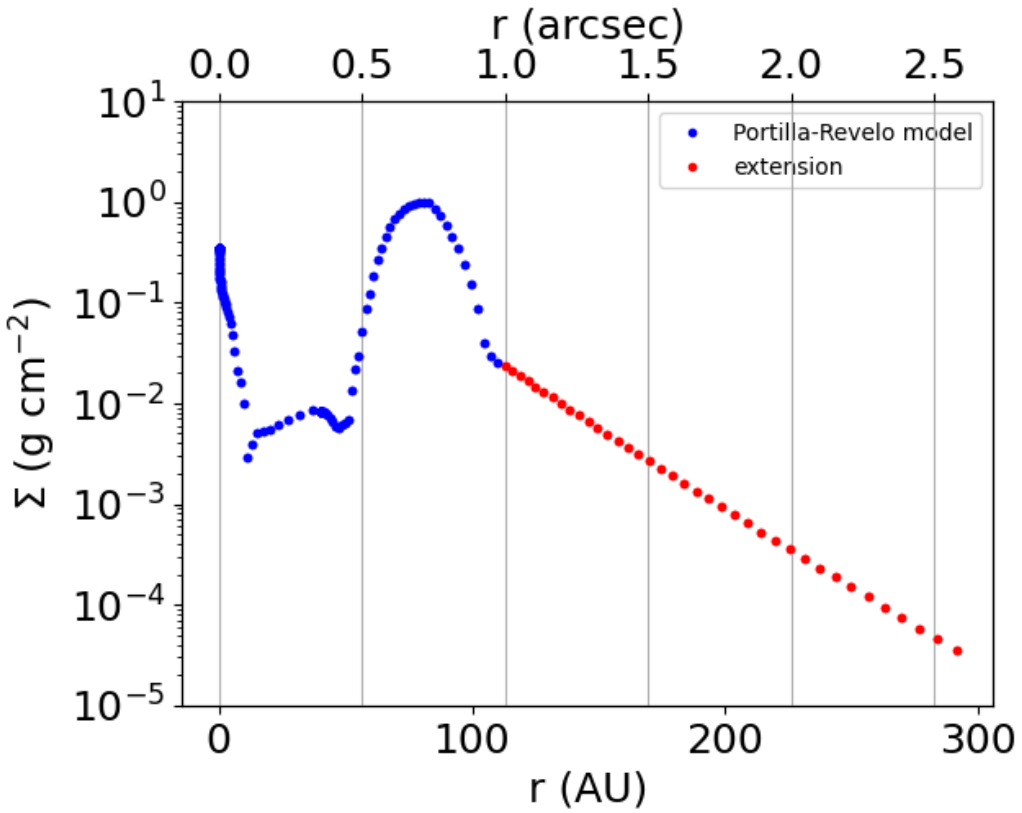

Figure 12: First guess gas surface density profile (iteration zero). A distinction is made between the Portilla-Revelo model (blue), which was not modified, and the extension (red) which was adapted to fit the $C^{18}O$ observations.

the critical density taken at 2.87 g cm^{-3}, and γ is the exponent of the power law which we set to 1 for this first guess (Cridland et al., 2023). For the dust, we simply assume that it follows the gas surface density:

$$\Sigma_{dust}(r, a) = \frac{\Sigma_{gas}(r)}{\Delta_{gtd}(a)}$$

where $\Delta_{gtd}(a)$ is kept constant at 10^5, taking into account 80 grain size bins. The radial line intensity profiles of three CO isotopologues were obtained (for the 2-1 transition) through the steps described in section 2.3, and were then compared to ALMA observations from Law et al. (2024) and Rampinelli et al. (2024).

C^{18}O, the most optically thin tracer, was chosen as the reference species used to build PDS-70's surface density profile. ^{12}CO and ^{13}CO radial profiles were obtained as well, but were used mainly as sanity checks and were not used in the correction process itself. In order to get an accurate flux profile for ^{12}CO, it needs parameters that describe the location of the emission due

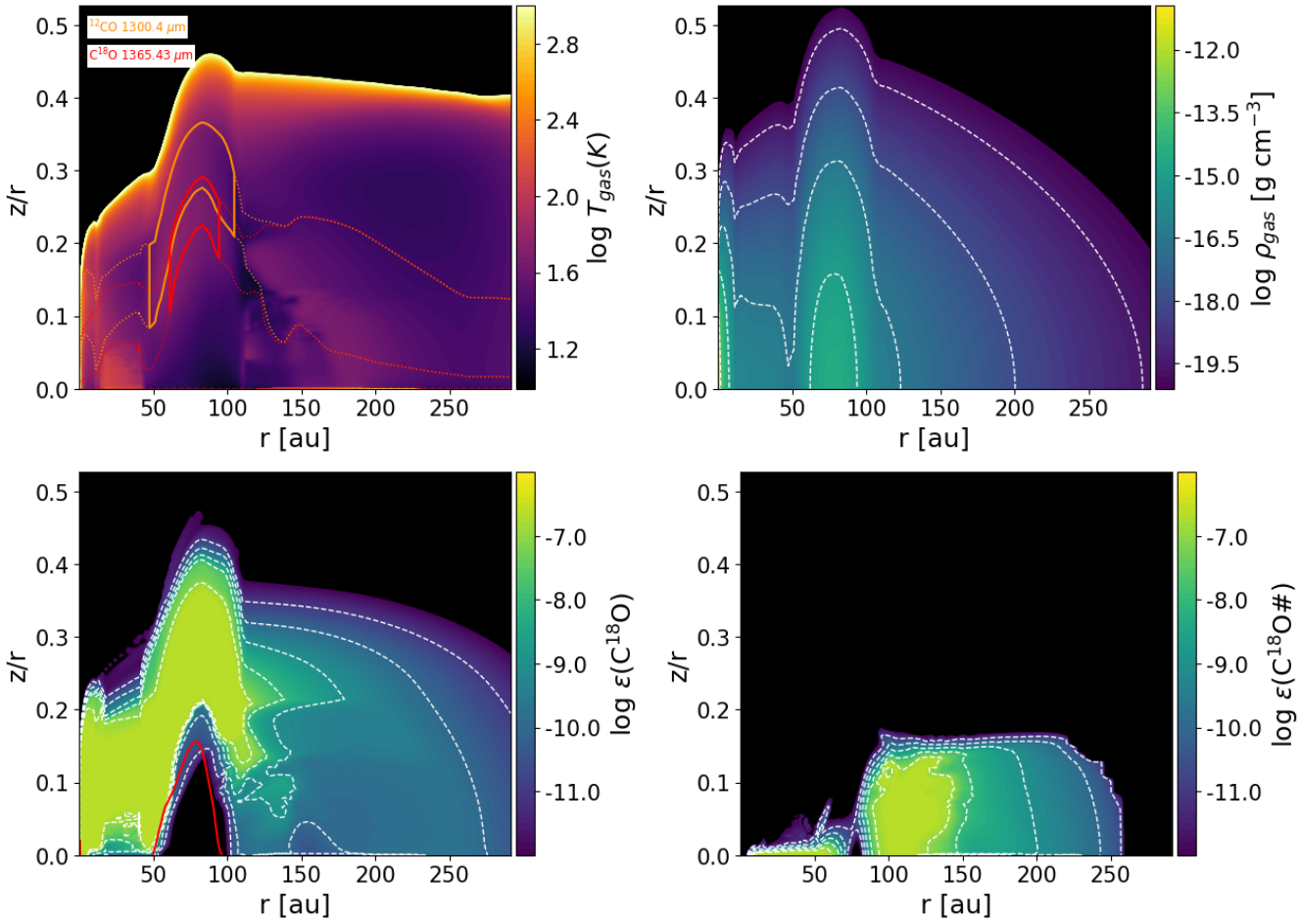

Figure 13: Top left: Line origin plot of the ^{12}CO (2-1) and C^{18}O (2-1) transitions on top of the gas temperature. The solid region indicates where $\sim$ 50% of the line flux comes from. We see that ^{12}CO emits overall higher in the disk due to being more optically thick. Top right: gas density contour. Bottom left and right: abundance contours (relative to H) of C^{18}O for the gas phase and the ice phase respectively. On the gas phase plot, an AV contour is also shown in red, indicating visual extinction for the gas.

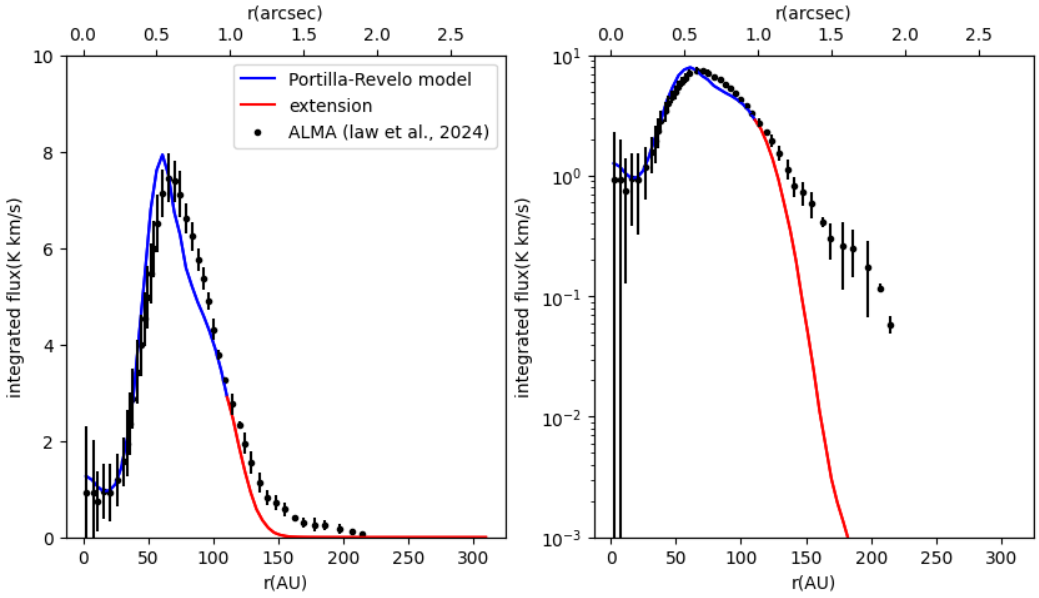

Figure 14: Iteration zero radial line intensity profiles for $C^{18}O$ (2-1) obtained using the steps of chapter 2.3, displayed both linearly and logarithmically for precise comparison between observation and model. The same distinction is made between the Portilla-Revelo model of the inner disk (blue) and the extension (red)

to its emission coming from further away from the midplane. These were obtained by using a model of the line-emitting surface as described in Law et al. (2024).

In figure 13 we see some structural aspects of our first guess model. In the outer disk, we see a smooth tapering off which is expected from an exponential density structure. We see that the ^{12}CO emits higher in the disk than the $C^{18}O$ which is expected due to ^{12}CO being more optically thick there.

In figure 14, the $C^{18}O$ radial profile of the iteration zero model is displayed in both a linear and logarithmic scale. It can be seen that in the iteration zero model, the flux is underestimated. Apparently, the observations of the outer disk do not agree with this model and it therefore it was adjusted.

3.2 The Iterative Procedure

To obtain a better fitting model, corrections were calculated radially by point-wise division of the observational flux by the model flux, and were then applied to our surface density profile by point-wise multiplication for each corresponding radial point. To ensure smoothness, a running median of four radial points was taken and then cubic splines were used to interpolate the surface density profile. This process was iteratively repeated until the $C^{18}O$ observations agreed with our model within at least three standard deviations.

Eventually a distance is reached for which no more observational data of the $C^{18}O$ line flux exists. This happens after approximately 220 AU for the Law et al. (2024) observations. To ensure that our model is not suddenly cut off, equation 7 is applied once again, and its parameters are estimated by eye in order to have the surface density profile taper off naturally.

In figures 15 and 16 the full evolution of the iterative procedure is displayed. Four iterations were needed to obtain a model which agrees with the observations within three standard deviations. More iterations were attempted, but these did not produce better fits.

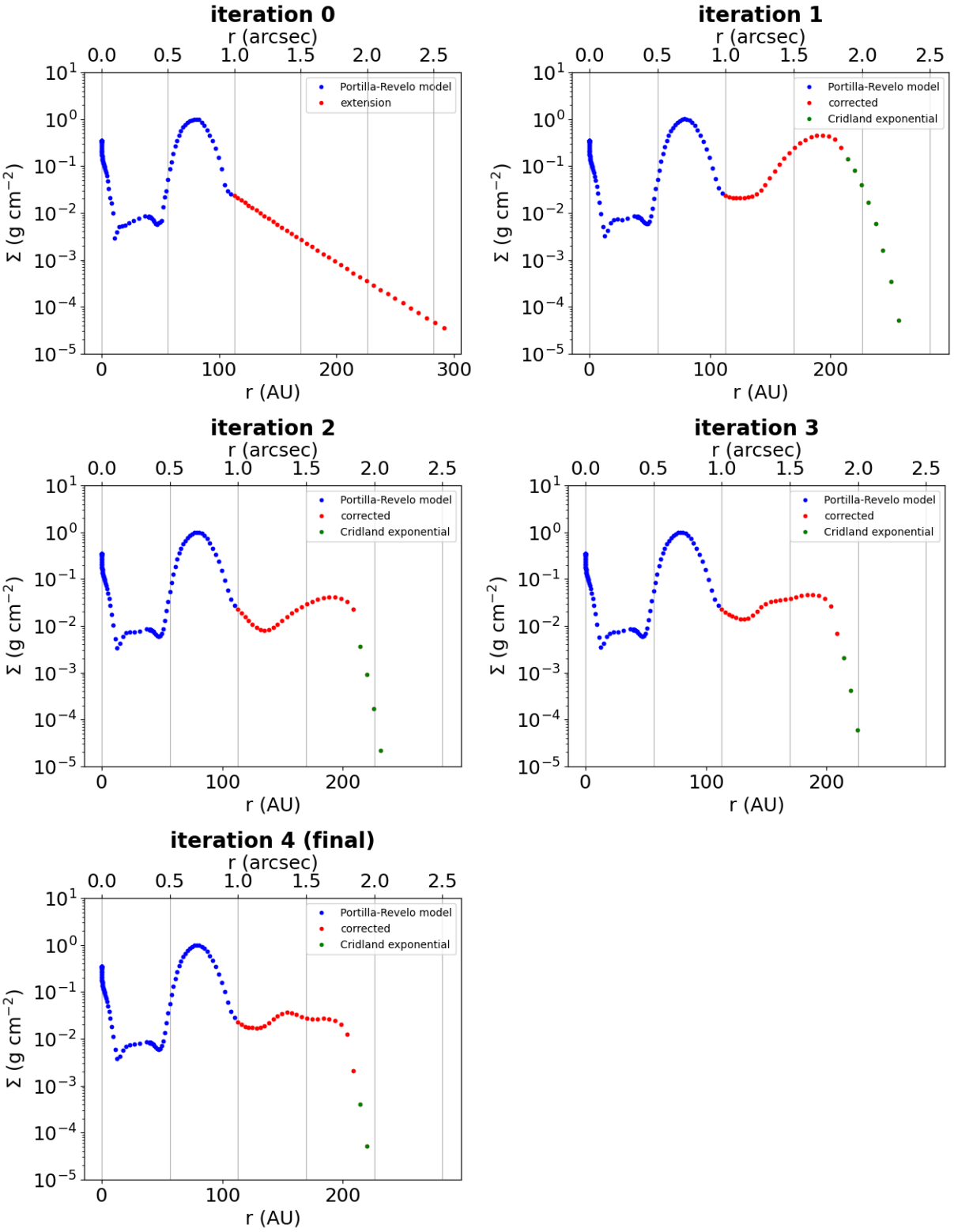

Figure 15: Full evolution of the iterative correction procedure for the surface density profile from iteration zero all the way to the final iteration.

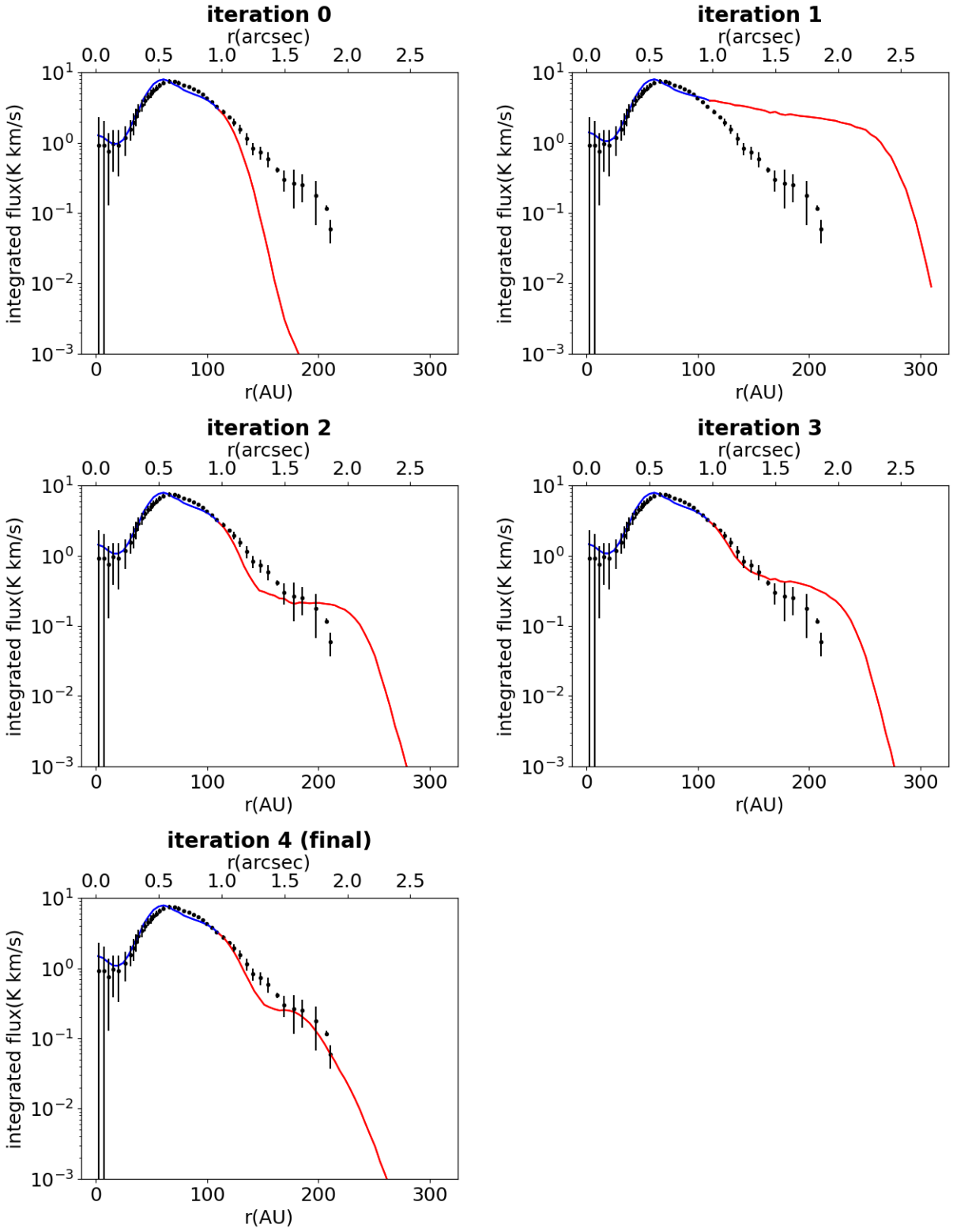

Figure 16: All the $C^{18}O$ (2-1) radial line intensity profiles corresponding to the surface density profiles of figure 15 displayed on a logarithmic scale. A distinction is made for the Portilla-Revelo domain (blue), the extended domain (red), and the observations from Law et al. (2024) (black dots).

3.3 The Final Model

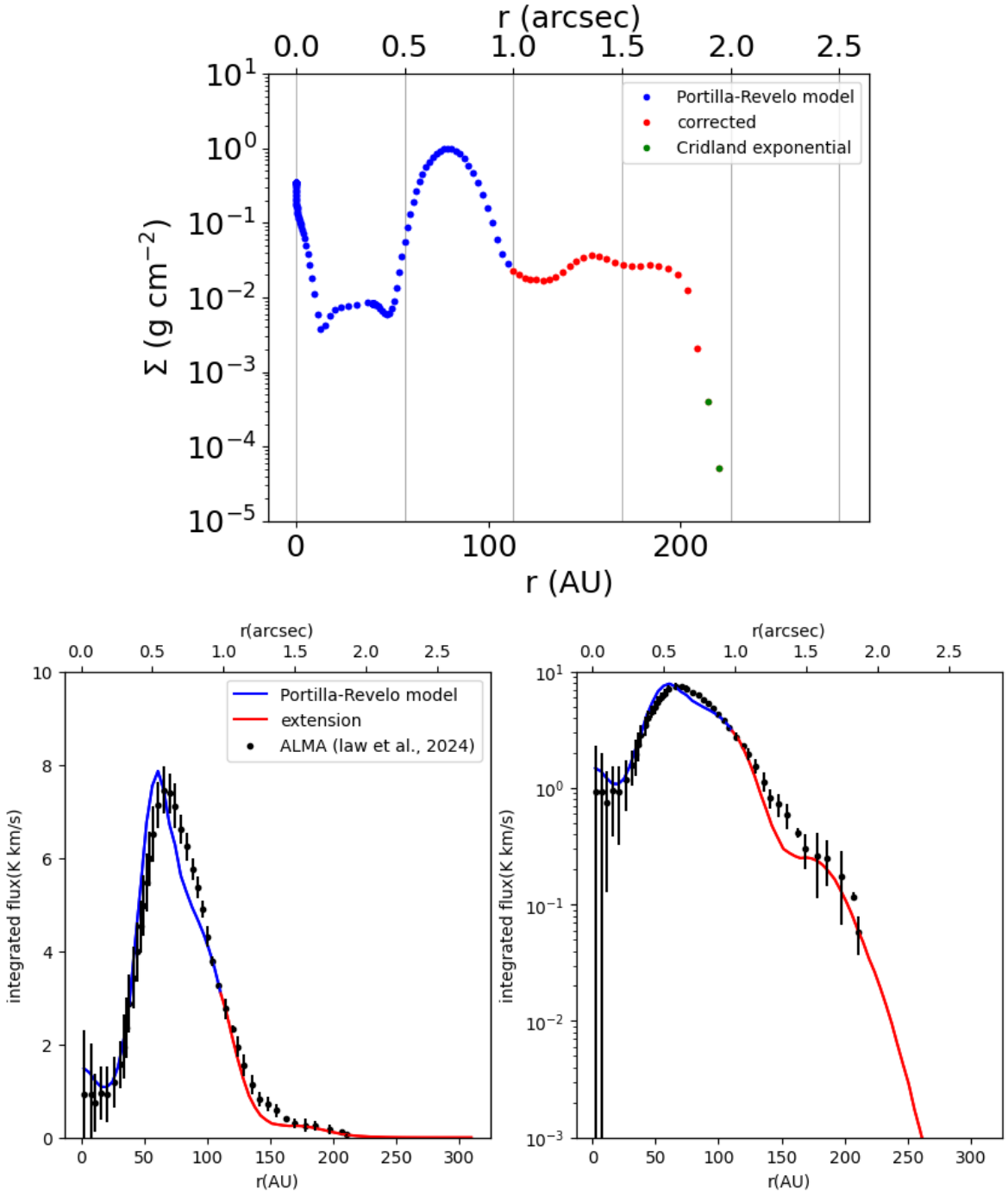

Figure 17: **Top**: surface density profile of the final extension model. Alongside the distinction between the Portilla-Revelo model (blue) and our extension, there is now also a distinction between the corrected points (red) and the points which were estimated by eye using equation 7 (green). **Bottom**: Radial line intensity profile for the $C^{18}O$ of the final iteration model obtained using the steps of chapter 2.3, displayed both linearly and logarithmically once again. The same distinction is made as in figure 14, between the Portilla-Revelo model of the inner disk (blue) and the extension (red).

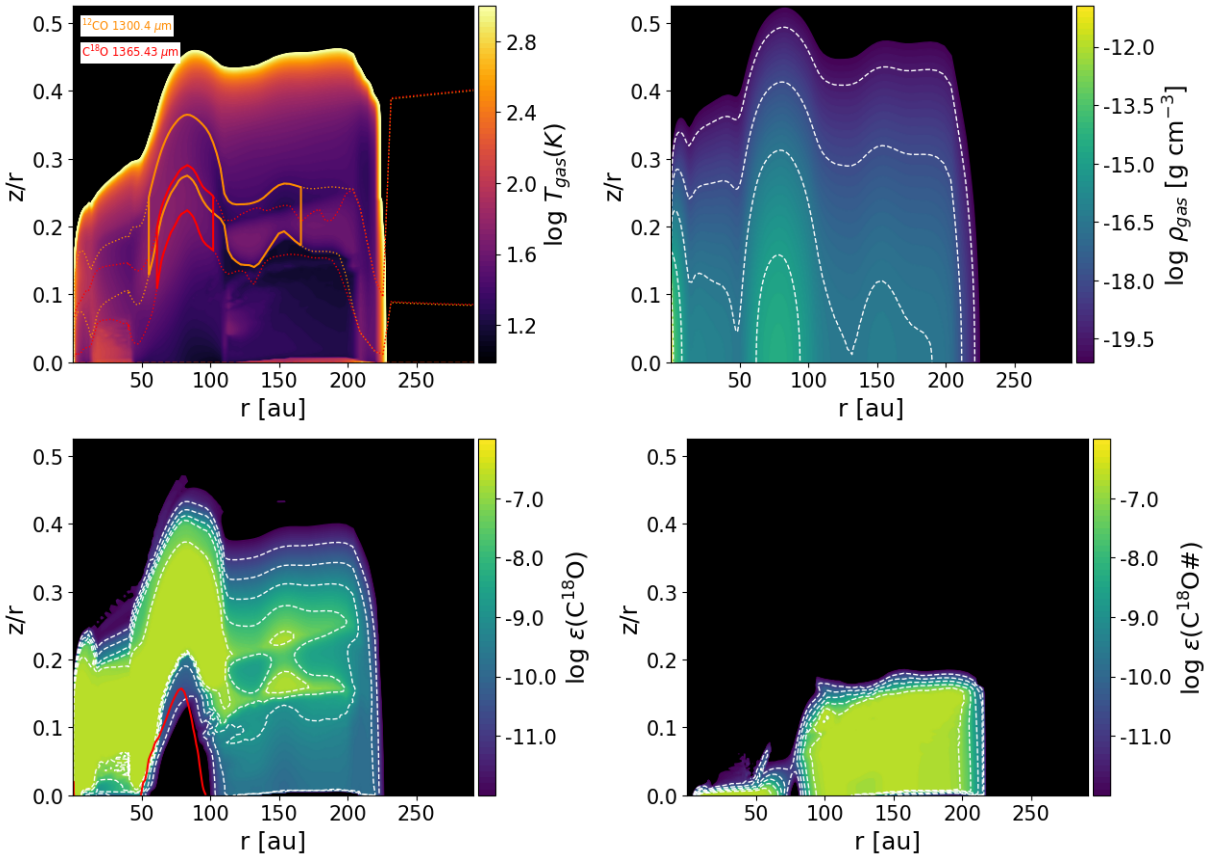

Figure 18: Contour plots similar to figure 13. This time they display the final model. The most noticeable changes are the plateau between 120 and 200 AU and the tapering off which is now much steeper.

After four iterations, the final surface density profile for our model is obtained. In the top plot of figure 17, the surface density profile of the final iteration is displayed. An interesting observation is that the surface density profile now appears to have a plateau stretching from approximately 120 AU (1 arcsec) to 200 AU (1.7 arcsec), where the gas surface density remains relatively uniform compared to the rest of the disk. Also noticeable is a slight dip in surface density between 100 and 150 AU.

The bottom plots of figure 17 show the final $C^{18}O$ radial surface brightness profile, which is now much closer to observation than the iteration zero model. Noticeable is a small kink in the profile at approximately 150 AU which is likely caused by limitations in the convergence of our iterative procedure (see discussion).

Figure 18 shows similar contour plots as figure 13, this time for the final model. The most striking change is that the smooth tapering off of iteration zero has now transitioned in a very steep drop in gas density at approximately 230 AU. This drop in gas density is more sudden than expected, especially since the observed radial profiles of ^{12}CO and ^{13}CO seem to taper off more smoothly (see figure 19).

Another noticeable change is a gas density plateau between 120 and 200 AU corresponding to the plateau in the surface density profile, where not only the $C^{18}O$ abundance remains relatively radially uniform, but also the temperature and gas density. The small dip between 100 and 150 AU is visible in the gas density and seems to correspond to a region of lower $C^{18}O$ gas abundance.

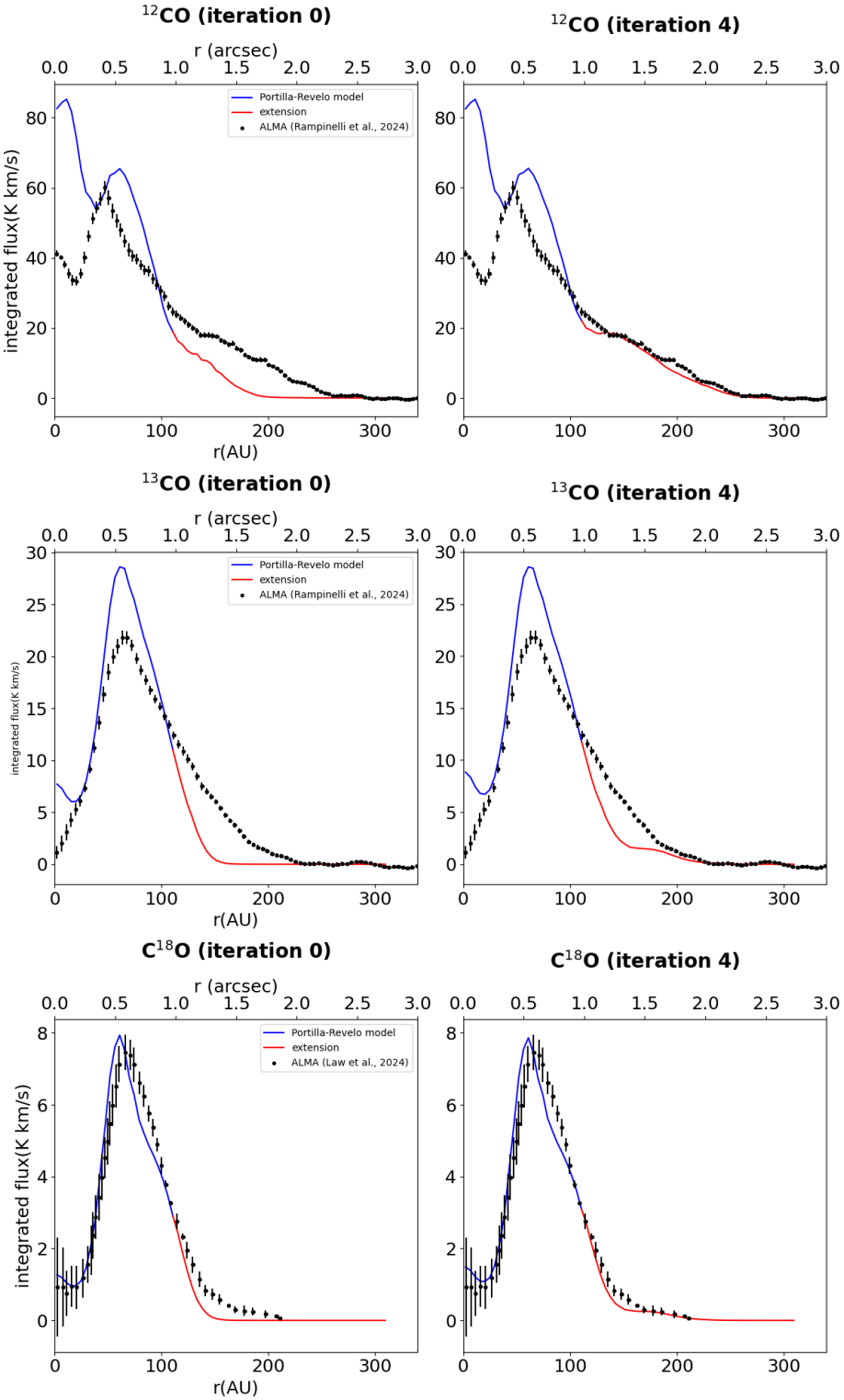

Figure 19: Radial line intensity profiles of all three CO isotopologues, comparing iteration zero to the final model. A distinction is again made between the Portilla-Revelo model (blue), the extenstion (red), and the observations (black dots).

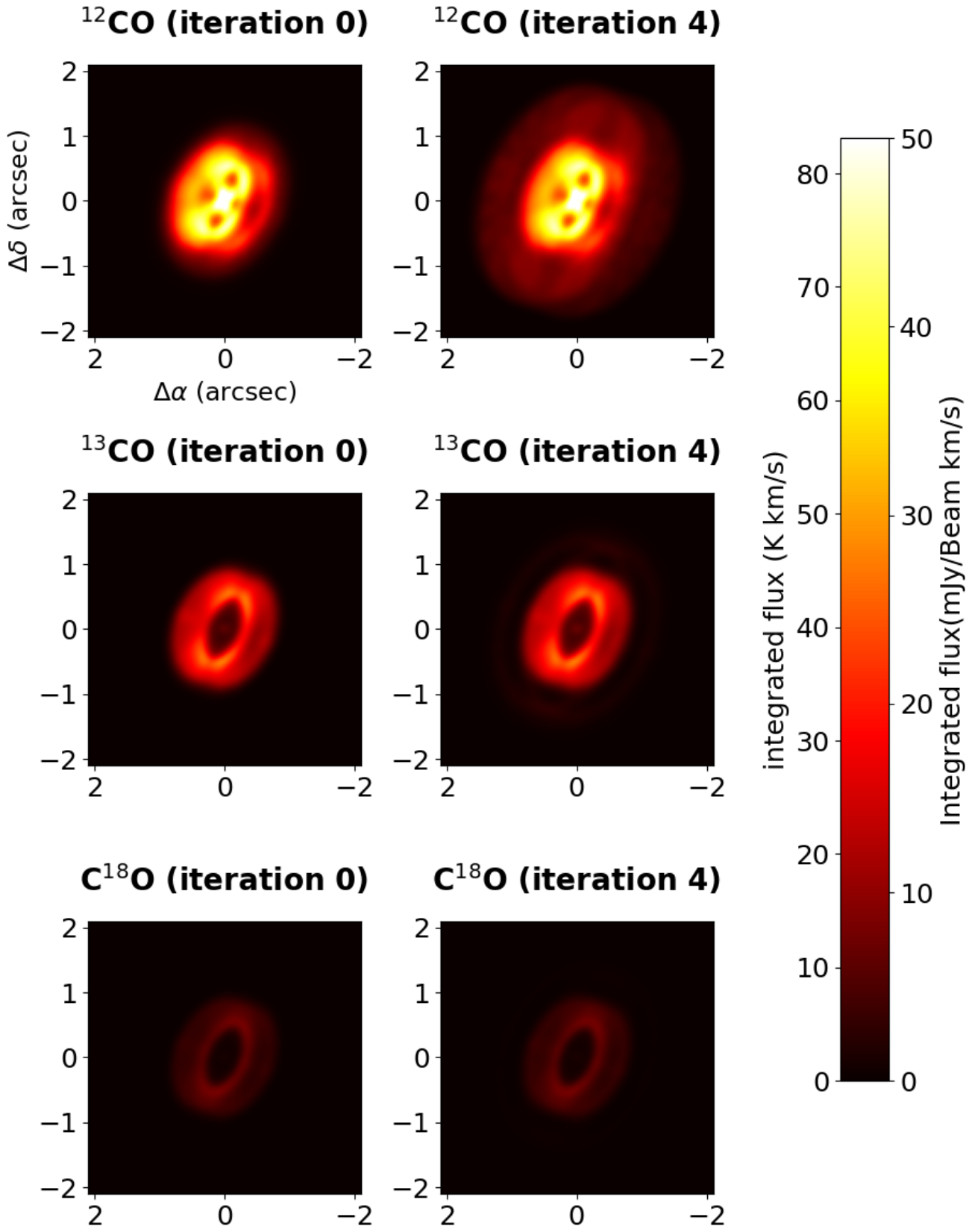

Figure 20: Moment-0 maps for all three CO isotopologues for iteration zero (left column) and the final iteration (right column). The plateau is clearly visible in the ^{12}CO moment-0 map

Close to the midplane (below $z/r = 0.15$ within the extended region) are overall lower temperatures than in the first guess model, resulting in more freeze-out of $C^{18}O$, which can also be seen in the ice abundance plot of figure 18, which has significantly increased, especially at distances from the star > 150 AU where ice abundance has increased by a few orders of magnitude. Interestingly, another dip in the $C^{18}O$ gas abundance is observed within the plateau at $z/r = 0.18$ and corresponds to a region of higher temperature.

In figure 19, radial surface brightness profiles are displayed for all the CO isotopologues. Figure 20 displays the corresponding moment-0 maps from which they were derived. Interestingly, ^{12}CO seems to fit quite well for the extension after correction even though the surface density was not corrected based on this isotope.

^{13}CO seems to display a 50 % overprediction of the surface brightness in the unmodified part (at ~ 80 AU) followed by a underprediction in the extended part between 120 and 200 AU. This underprediction does not seem to improve much with the corrections.

4 Deriving the C/O Ratio with C_2H

Now that the final disk model has been obtained, the next step is to derive the C/O ratio in the outer disk by looking at the C_2H (3-2) line. This was done in similar steps as the $C^{18}O$, namely by generating synthetic line observations for the C_2H transitions displayed in table 1 and fitting them to observations to within at least three standard deviations. This time however, instead of the surface density profile, the C/O ratio was varied. The $C^{18}O$ radial profiles were studied as well. This was done to check whether altering the C/O ratio affects the $C^{18}O$ abundance to such a degree that it destroys the fit.

Figure 21 displays the C_2H radial profile for the final model of the previous chapter, which assumes a C/O ratio of 0.46, showing that the C_2H is severely underestimated. Therefore, this C/O is too low and needs to be increased. This was done in two ways: by depleting oxygen and by adding carbon.

Cridland et al. (2023) used a similar approach to study the C/O ratio of PDS-70 and find a C/O of 1.01 (through oxygen depletion). Therefore, to also compare results from our approach to theirs, the C/O in our model was increased to this value, as well as a more extreme value of 5.

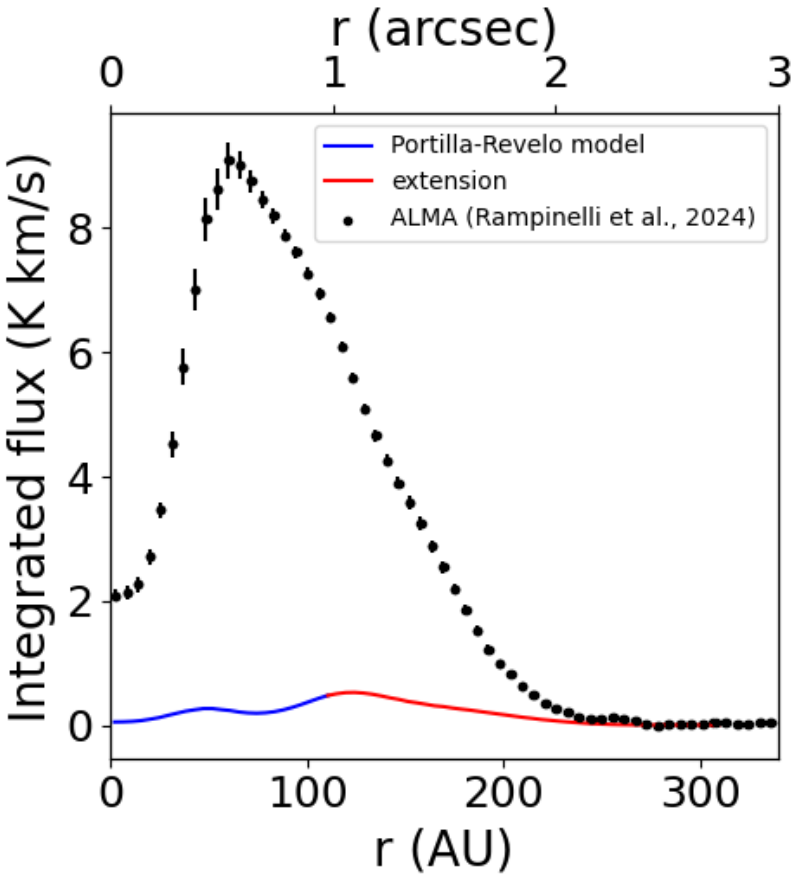

Figure 21: Radial integrated flux profile of the (co-added) C_2H (3-2) line of the final iteration model for a C/O ratio of 0.46. A distinction is once again made between the unchanged radial region (blue) and the extended region (red). The observations from Rampinelli et al. (2024) are shown as black dots with error bars.

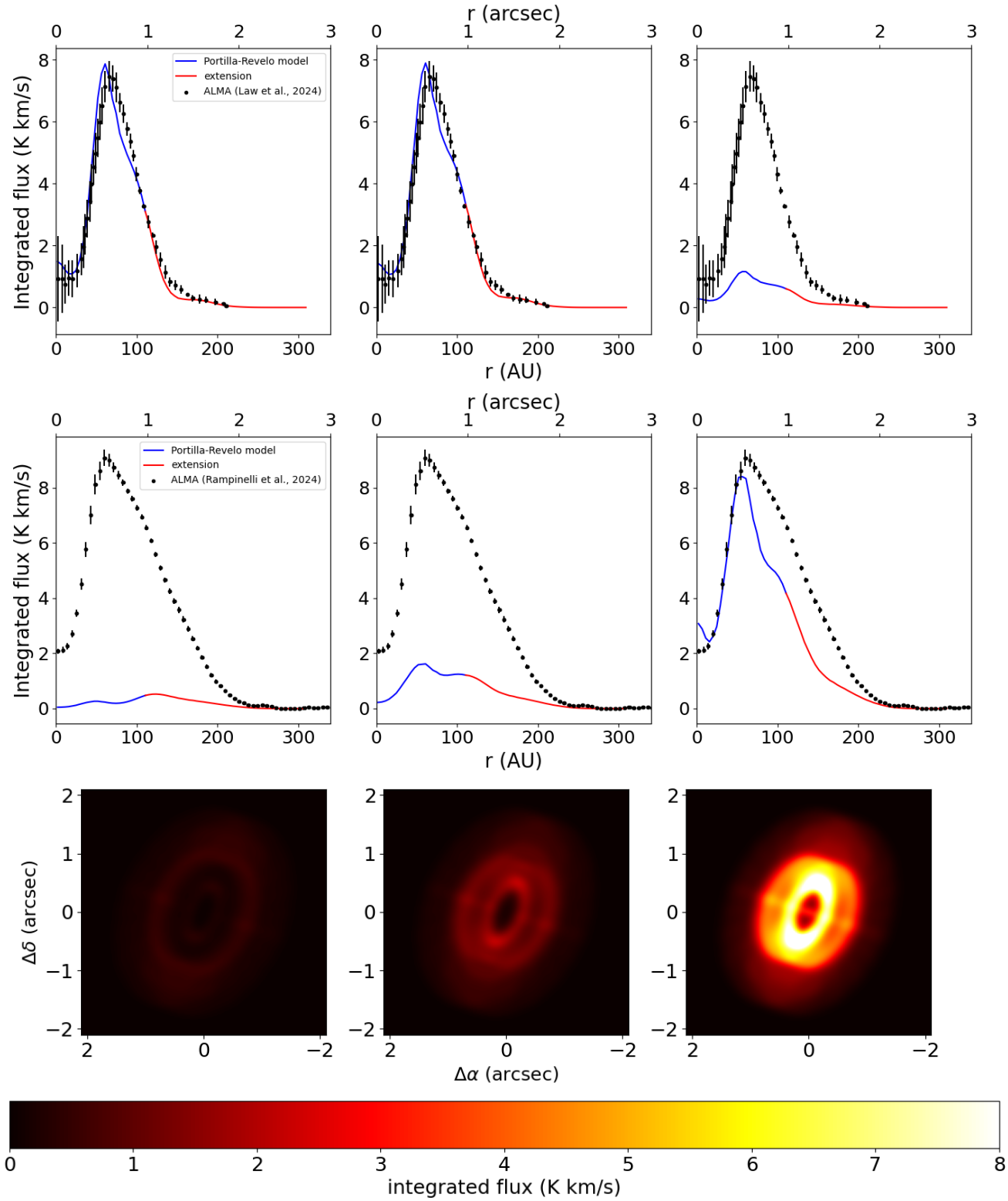

Figure 22: Radial integrated flux profiles profiles for the $C^{18}O$ line (top row), and the C_2H line with the corresponding moment zero maps (middle and bottom rows). The columns show three different C/O values (0.46, 1.01, 5) which were obtained through depletion of oxygen.

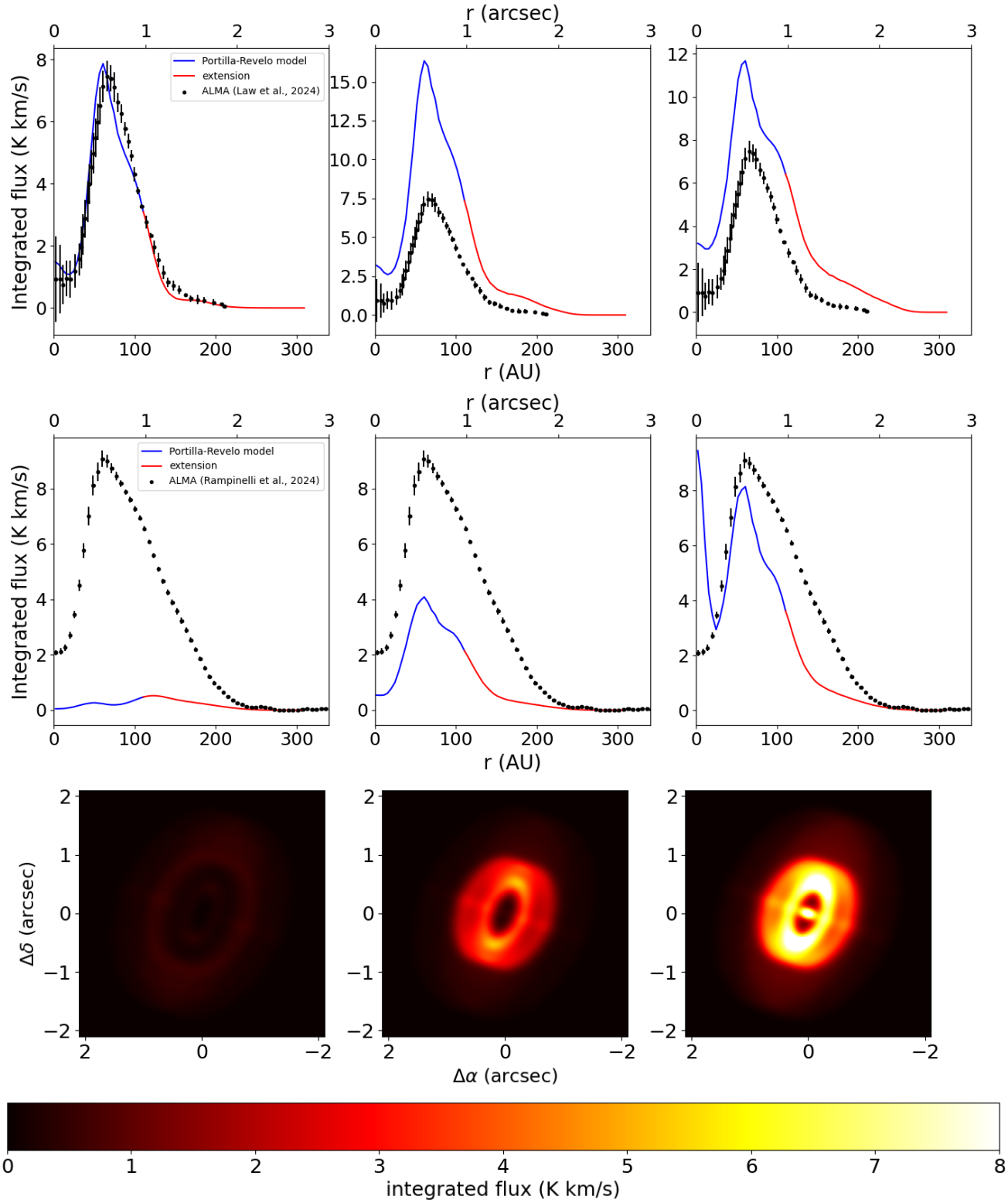

Figure 23: Radial integrated flux profiles profiles for the $C^{18}O$ line (top row), and the C_2H line with the corresponding moment zero maps (middle and bottom rows). The columns show three different C/O values (0.46, 1.01, 5) which were obtained through addition of carbon.

In figures 22 and 23, radial profiles for C_2H along with their corresponding moment zero map, as well as the radial profiles for $C^{18}O$, are shown for the final iteration model where the C/O ratio has been varied in the two by oxygen depletion and carbon addition respectively.

In order to retrieve radial profiles which are somewhat comparable to observation, the C/O must be raised to a value of 5. In the extended region, even this value is still too low to produce a fit within at least three standard deviations of the observations. This is true for both oxygen depletion and carbon addition, which produce similar results for the C_2H. However, the $C^{18}O$ flux was affected significantly as well. In the case of oxygen depletion, we see from figure 22 that the $C^{18}O$ flux is not visibly affected if the C/O is raised to 1.01. However, when it is raised to 5 we can see that it is consistently lowered by approximately a factor 8.

The $C^{18}O$ flux is more sensitive to the variation of the C/O ratio if carbon is added (see figure 23). For a C/O of 1.01 the flux is already increased by a factor of 2 with respect to the observations. However, when the C/O is raised to 5, the flux decreases again, such that it deviates from the observations by a factor of approximately 1.5.

Noticeable as well in our model is that the C_2H flux increases faster with the C/O in the region < 70 AU than in the region beyond this radius. This can also be seen in figure 24. 50% of the line emission (the solid region) is concentrated beyond 100 AU for C/O = 0.46. As the C/O is increased through either method, the bulk C_2H emission migrates further radially inward, indicating two separate regimes for the increase. This means that further increase of the C/O

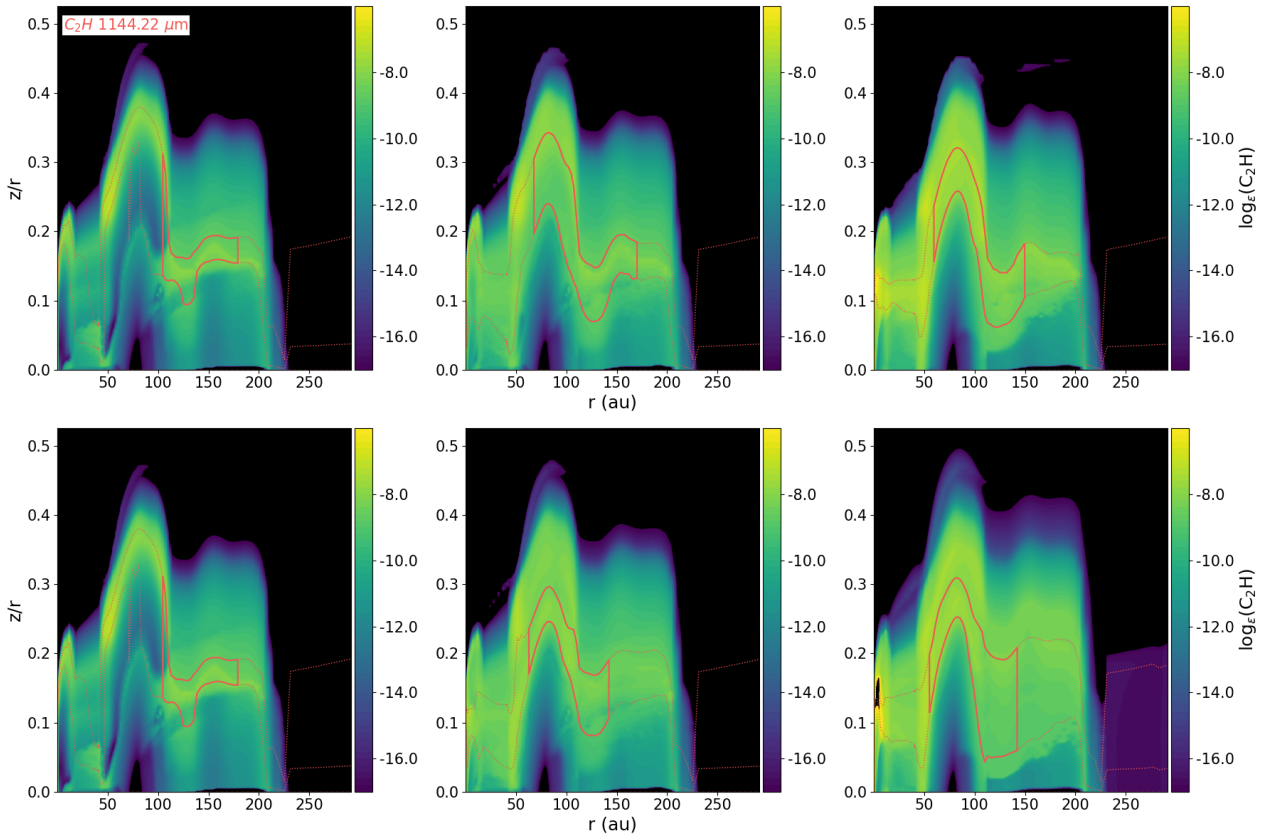

Figure 24: Changes in the line emitting region for C/O values of respectively 0.46, 1.01 and 5 through oxygen depletion (top row) and carbon addition (bottom row) on top of the C_2H abundance (relative to hydrogen). The solid region indicates where 50% of the line emission is coming from.

above 5, while it might produce a better fit in the extended region, would destroy the fit in the inner region in both cases. For this reason, as well as the $C^{18}O$ flux being affected too much, higher values for the C/O were not modeled at this stage.

Lastly, we see that the C_2H results, while similar, are not entirely symmetrical for both methods of increasing the C/O. While the intermediate C/O case produces C_2H fluxes that are different between the two methods, a C/O of 5 leads to very similar C_2H flux profiles. The only notable exception is at radii smaller than 30 AU, where the C_2H flux is significantly stronger for the carbon addition results.

5 Discussion

The procedures described in the previous two chapters yielded interesting and sometimes surprising results. In this chapter I will discuss both procedures separately, starting with the fit of the $C^{18}O$ (2-1) line flux (and of the other isotopologues) and the interesting surface density profile of the final model (the plateau and the under-abundance of $C^{18}O$ at z/r = 0.18). I will also discuss the C/O ratio, comparing our results with those of Cridland et al. (2023) and explain the differences.

5.1 Evaluating The Final Surface Density Model

5.1.1 The Fit of the CO Isotopologues

Figure 19 shows that the model fits the $C^{18}O$ and the ^{12}CO observations within three standard deviations of the observations for the extended region. However, the ^{13}CO does not. The change in the surface density profile was too small to change the ^{13}CO flux enough to produce a fit within these parameters. ^{13}CO, being on the edge between optically thick and optically thin, may be the most difficult isotopologue to fit because it reacts to both temperature and column density, making results more unpredictable. The ^{12}CO is optically thick, and therefore sensitive to changes in the temperature structure between the starting model and the final model, temperatures lowering about an order of magnitude in the outer disk.

Figure 19 shows an overestimation of the ^{13}CO (2-1) flux in the unaltered region, and an underestimation in the extended region. Important to note is that in this project, isotope specific chemistry was not included. Constant isotope ratios are assumed for carbon and oxygen, which remain unchanged throughout the iterative process. This can cause overestimations and underestimations of molecular abundances.

Important to note is that for the iterative correction process, more iterations do not necessarily result in a better converging surface density profile. The relation between the line flux and the surface density is non-linear, as many steps are needed to derive the line flux from the surface density profile (see chapter 2.2) and changes made in the surface density can cause unexpected changes in the flux.

5.1.2 The Plateau and the CO Depression

Interestingly, the final surface density profile (see figure 17) has a sharp decline at a radius of 100 AU which then forms a plateau which spans approximately 80 AU radially, after which the gas density sharply tapers off. The plateau can also be seen in the thermal structure of the model (figure 18 top left), which also displays a fairly uniform vertical pattern throughout the plateau. This is an unexpected result compared to observations of disks from the MAPS survey which included T-Tauri disks similar to PDS-70 as well as the more massive Herbig Ae/Be counterparts (Miotello et al., 2022; Brittain et al., 2023; Zhang et al., 2021). The gas surface density profiles derived for the disks of this survey taper off more smoothly.

The strange surface density shape of our PDS-70 model and the kink in the $C^{18}O$ flux may be caused by limitations in the iterative procedure. For example, the only parameter that was varied in the procedure was the surface density profile. All other parameters were assumed to be constant. Secondly, correction factors obtained from comparing the synthetic $C^{18}O$ flux profiles to the observed ones were linearly applied to the surface density profile. The process of obtaining the synthetic observations from the surface density profile is very non-linear, as it involves many steps in between (See chapter 2.2).

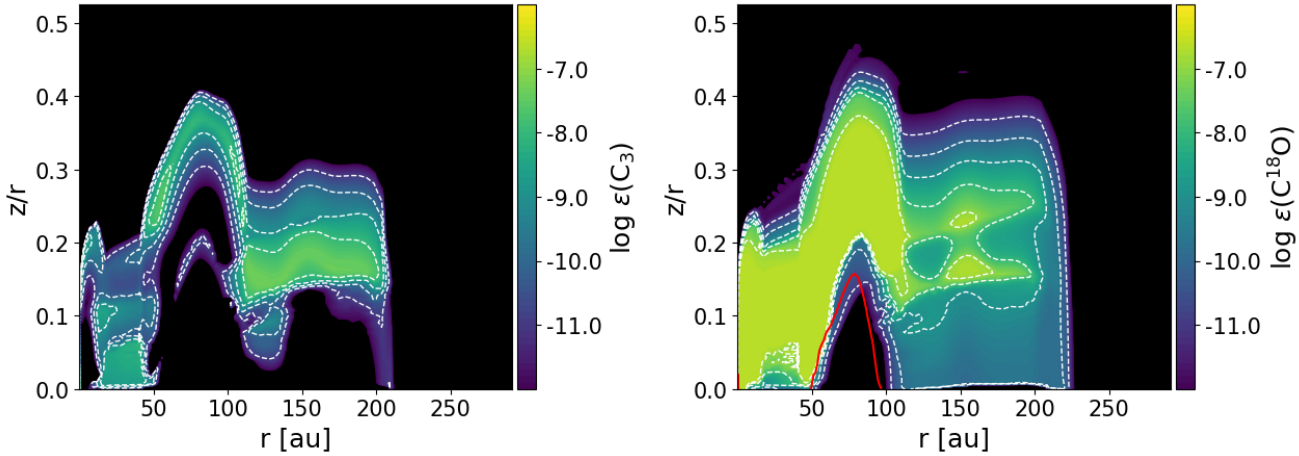

Figure 25: Abundance plots for respectively C_3 and $C^{18}O$ for the final model. In the region of the $C^{18}O$ depression ($z/r \approx 0.18$ and 120 AU $< r <$ 200 AU) C_3 is most abundant and even dominates the $C^{18}O$ abundance by an order of magnitude, indicating a different carbon chemistry and less efficient cooling in this area.

Also noticeable is a depression of about two orders of magnitude in the $C^{18}O$ abundance between 120 AU and 200 AU at z/r = 0.18 in figure 18. This depression also exists for the other CO isotopologues and corresponds to a region of higher temperature. This indicates less efficient cooling in this area. Figure 25 further confirms this by showing that for example the molecule C_3 peaks in the region where $C^{18}O$ abundance is lower. This indicates that carbon atoms in this region are more likely to form C_3 molecules, causing a depression in the CO abundance and thus less CO-cooling. This explains the higher temperature. However, it is not clear if the higher temperature is the cause of the depression or its effect, as the chemistry and the heating/cooling balance are coupled (see chapter 2.2.4).

5.1.3 The Gas-to-Dust Mass Ratio

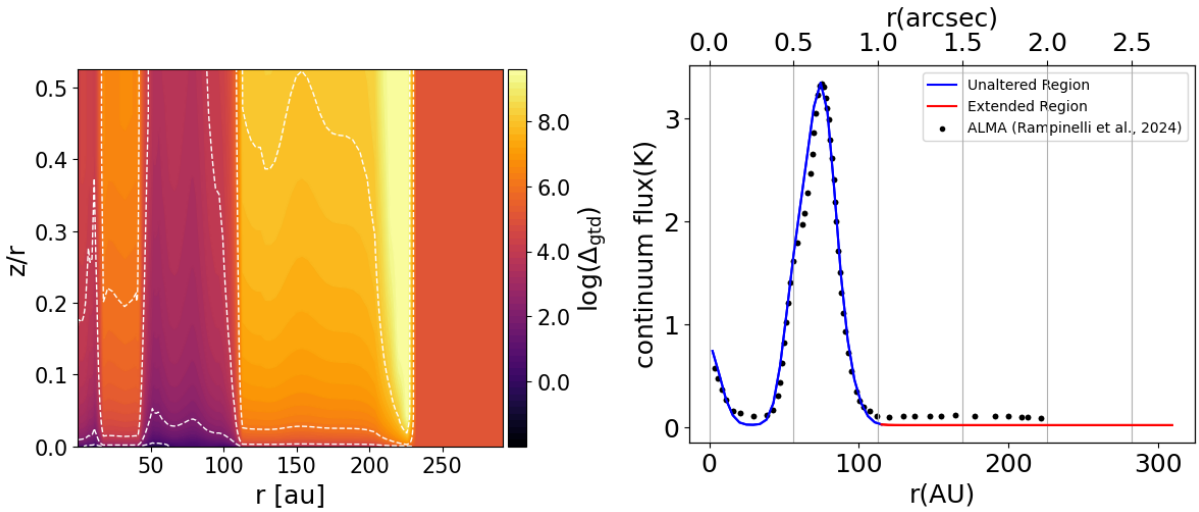

Figure 26: Left: gas-to-dust mass ratio throughout our final iteration model of PDS-70. Right: radial surface brightness profile of the 855 μm dust continuum emission.

An important assumption in this model is that throughout the extended region, the gas-to-dust mass ratio is kept more or less radially constant in the input surface density profile. The dust surface density profile therefore follows that of the gas. It is also assumed to be very high, from 10^5 at the midplane to as high as 10^9 at larger z/r values (see figure 26), so that the dust abundance relative to the gas is negligibly small. This assumption is made because continuum observations do not show any dust emission in the extended region (see figure 26 and also the continuum brightness profile from Rampinelli et al. (2024)). Figure 26 shows a more detailed 2d contour map of the gas-to-dust mass ratio throughout our final model. Throughout the extended region, the gas to dust ratio reaches as high as 10^8 in the upper layer due to dust settling. In this work it is also assumed that our assumed dust abundance is below the 3σ upper limit from ALMA (figure 26).

However, the fact that there is no observed dust emission does not mean that there is no dust in the extended region. It is simply unknown how much there is. It is important to obtain more information about the dust abundance in PDS-70's outer regions through for example more sensitive observations. Continuum emission may exist in these regions, but may be too weak to pick up because of very low dust temperatures and column densities, as the dust emission scales with both of these parameters (Isella et al., 2019; Rampinelli et al., 2024). It is important for future models to check whether altering the dust abundance changes the CO or C_2H emission, as small amounts of dust emission at this distance may influence the gas emission.

5.2 Evaluating the C/O Results

5.2.1 Comparing our C/O Results to the Literature

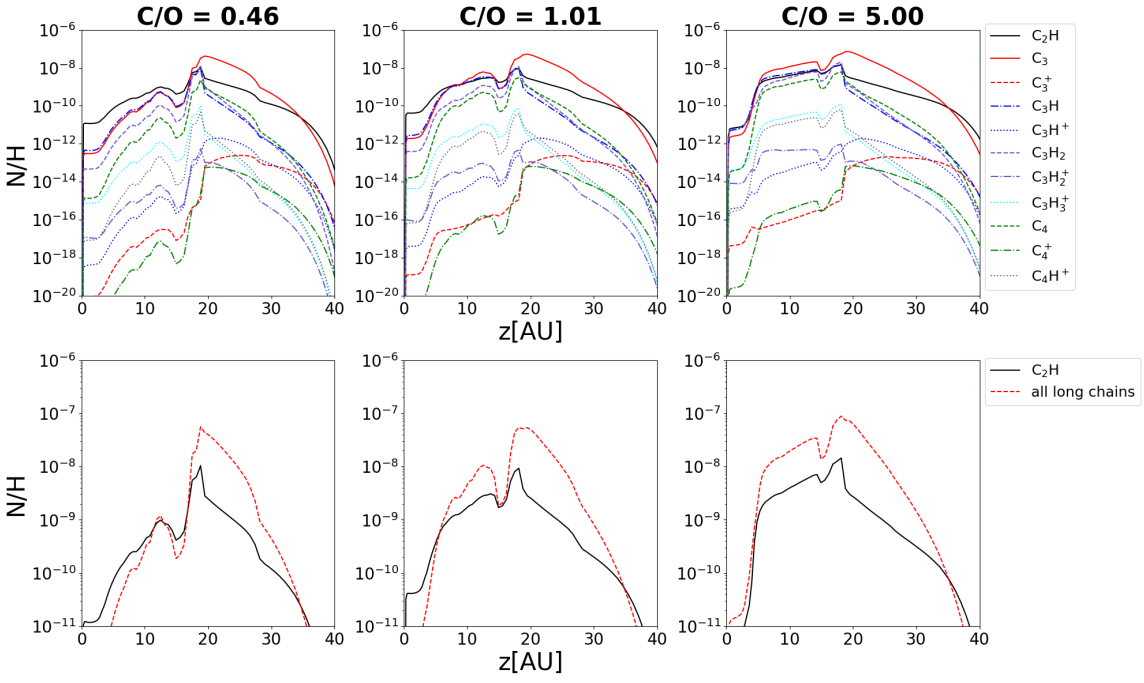

Figure 27: Vertical abundance slices of hydrocarbons at a radius of 130 AU from the star for three different C/O ratios obtained from depletion of oxygen. The top row shows the C_2H along with all the longer chain hydrocarbons used in the model individually. The bottom row shows all the long chain hydrocarbon abundances, which were co-added, compared to C_2H. The abundance is relative to hydrogen.

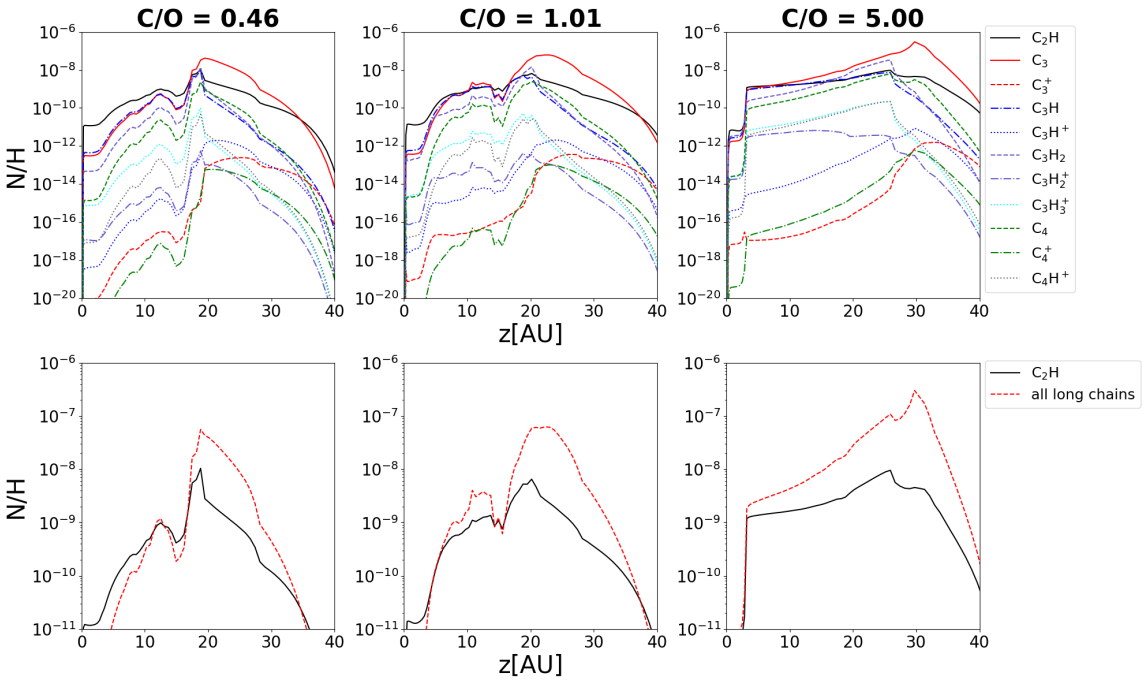

Figure 28: Vertical abundance slices of hydrocarbons at a radius of 130 AU from the star for three different C/O ratios obtained from addition of carbon. The top row shows the C_2H along with all the longer chain hydrocarbons used in the model individually. The bottom row shows all the long chain hydrocarbon abundances, which were co-added, compared to C_2H. The abundance is relative to hydrogen.

In order to match the C_2H line observations of PDS-70, the C/O ratio needs to be raised to a value of approximately 5, in the case of both oxygen depletion and carbon addition. If we compare our framework to that of Cridland et al. (2023), the result is surprisingly different, as their framework favored a disk model with a C/O ratio of 1.01.

In order to explain this difference, the chemical networks of both models were compared. The framework of Cridland et al. (2023) uses the DALI code, which simulates proto-planetary disk chemistry in a similar way as ProDiMo, by solving the rate equations. However, there are differences in the chemical network itself.

Our model uses the chemical network described in Kamp et al. (2017), which consists of 250 species (without isotopologues) built from 13 elements connected through 3171 reactions. The chemical network of Cridland et al. (2023) is described in Visser et al. (2018) and consists of 281 species (including isotopologues) and 5751 reactions. More specifically for the C_2H, our framework has 79 reactions that involve the destruction and production of this molecule, whereas their network has 64. Neither our nor their network includes isotopologues for the C_2H. Although this is not a major difference for the C_2H, the reaction network is not entirely the same. The inclusion of isotope specific chemistry in their network for example, affects the abundance of other molecules, which in turn affects the heating/cooling balance, which can result in different reaction rates for the C_2H as well.

Cridland et al. (2023) state that longer chain hydrocarbons (any molecule with more than two carbon atoms) are not included in their framework. They discuss that this would result in an over-prediction in the C_2H as the carbon atoms not bound to CO would tend to favor these longer chains in the inner disk (< 5 AU), but that the outer disk would be largely unaffected. We

can check this in our model because it does include these long chain hydrocarbons. Figures 27 and 28 show vertical abundance slices of C_2H and the long chain hydrocarbons in the outer disk of PDS-70 for the three different C/O ratios in our model, encompassing both methods of C/O increase. These figures show that in the outer disk, the abundance of the long chain hydrocarbons (particularly C_3) is approximately an order of magnitude larger than the abundance of C_2H and tends to increase faster than the C_2H abundance as we increase the C/O ratio through oxygen depletion. The same is true for carbon addition. This shows that the carbon not bound to CO indeed favors the longer chains over C_2H, even in the outer disk. Therefore, the assumption that the outer disk is largely unaffected by the longer chains is not justified for our model of PDS-70. It is clear from this work that their presence affects the estimate of the C/O ratio significantly in the outer disk.

5.2.2 The Effect of the C/O ratio on the CO and C_2H Line Emission

The increase of the C/O ratio much beyond the value close to 1 has a larger effect on the CO flux than expected. If the C/O is increased to 5 through oxygen depletion, the $C^{18}O$ peak flux decreases by a factor 8 (see figure 22, top right). If carbon addition is the method applied, the $C^{18}O$ peak flux increases by a factor 1.5 (see figure 23, top right). This reaction of the $C^{18}O$ line is asymmetrical because the carbon and oxygen abundances affect the temperature structure in the disk model differently. It is unclear which of the two methods of C/O increase is preferred. Both methods yield results that are similar for the C_2H, but carbon addition does not affect the $C^{18}O$ flux as much.

For both methods it is necessary to go back to the surface density profile and rebuild it again to match the $C^{18}O$ radial intensity profile at a C/O ratio of 5. This may result in an altogether different value for the C/O ratio as well. It may therefore be necessary to go back and forth between building the surface density profile and fitting for the C/O ratio in an iterative process in order to find the best fit for both molecules. Doing so for both methods of C/O increase could also help determine which of the two methods is preferred for our model.

Increasing the C/O ratio also affects the C_2H line emission and abundance in unexpected ways. The C_2H radial surface brightness profiles of figures 22 and 23 do not increase uniformly with the C/O ratio throughout the entire radial extent of the disk. Instead, the inner disk flux (< 100 AU) increases much faster than the flux beyond this radius. This is further illustrated by figure 24, which shows that the bulk of the line emission, while first concentrated beyond 100 AU, spreads further inward due to the abundance increasing much more quickly in the region inward of 100 AU.

This is an important observation because in our model the C/O ratio is increased uniformly throughout the disk. While a C/O ratio of 5 might fit the C_2H below 70 AU, it may need to be much higher beyond this radius to match C_2H observations there. It is therefore unlikely that a uniform C/O ratio will produce a good fit for the C_2H line flux throughout the entire disk. A suggested next step would therefore be to separate the model into zones with different C/O ratios to see if this would improve the fit in the outer disk.

5.2.3 The Robustness of our derived C/O Value

As a final point of discussion it is important to consider whether a C/O ratio of 5 is a realistic result. While long-chain hydrocarbons explain why the C/O needs to be raised so much higher in our model than in that of Cridland et al. (2023), it does not explain the underlying physics behind this ratio in PDS-70 or how realistic it is.

Studies of time-dependent models of proto-planetary disks such as the one described in Krijt

et al. (2020) suggest that taking into account dust coagulation and pebble dynamics can affect the C/O in the outer disk significantly. In the outer disk midplane, nearly all of the C and O has frozen out into ices. However, at larger scale heights, the picture is much different. Most of the ices tend to be rich in oxygen, meaning that much of the gas is oxygen depleted. A lot of this ice is moved inwards, meaning that the C/O increases much above 1 over time. High above the midplane, values of 5 and above are therefore not unrealistic, even just for the gas (see for example Krijt et al. (2020), figure 10).

While pebble accretion is not taken into account in either our model or that of Cridland et al. (2023), it still may serve as an explanation why observations tend to favor such a high value for the C/O. However, it is too early to tell whether this value of the C/O is correct, or if a uniform C/O is even enough to produce a good fit with observations.

6 Conclusion

In this work, the model described in Portilla-Revelo et al. (2021) and Portilla-Revelo et al. (2023) has been radially extended beyond 120 AU in order to derive the gas C/O ratio of PDS-70 in the outer disk. Using ProDiMo to calculate the disk structure and chemistry, and both CASA and GoFish for the post-processing and comparison to ALMA observations, a surface density profile was iteratively built for the outer disk gas, through comparing simulated $C^{18}O$ radial flux profiles to those obtained from ALMA observations (Law et al., 2024).

A surface density plateau between 120 to 200 AU from the star is observed. In this range, both the gas density and temperature remain relatively constant, except within a region of lower CO abundance at z/r = 0.18, where temperature is increased due to less efficient cooling. This is very different from most other disks, which seem to favor am exponential tapering off (Miotello et al., 2022; Brittain et al., 2023; Zhang et al., 2021).

An important caveat is that the dust abundance in the outer disk is assumed negligible compared to the gas, with the gas-to-dust ratio assumed to be more or less radially constant at 10^5. This assumption was made because no 855 μm continuum dust continuum emission has been detected beyond a radius of 80 AU. However, it is not known how much dust there actually is in the area. The non-detection of continuum emission can also be caused by low dust temperatures and densities. This can affect the gas emission. In order to obtain more robust results, the effects of the dust need to be studied in future models by for example varying the gas-to-dust ratio. If this results in significantly different emission for the gas, deeper continuum observations are needed to constrain the dust density in PDS-70's outer disk.

To derive the C/O ratio in the outer disk gas, C_2H radial surface brightness profiles were studied. This was done by varying the C/O in a similar way as Cridland et al. (2023). Depletion of oxygen and addition of carbon were the methods used, which were separately applied and then compared. Our model favors a C/O well above 1 for both cases, with a C/O of 5 producing results that agree most with observations. However, for a C/O this high, The $C^{18}O$ fit is destroyed, lowering by a factor 8 for oxygen depletion, and increasing by a factor 1.5 for carbon addition. Because of this, and also because higher values of the C/O would destroy the C_2H fit in the inner disk due to its abundance increasing faster there, C/O ratios above 5 were not modeled.

Compared to the model from Cridland et al. (2023) Our model is significantly less abundant in C_2H. This is because our chemical network also includes longer chain hydrocarbons (more than two C-atoms) which tend to have an order of magnitude higher abundance. This results in our model favoring a C/O ratio five times higher than theirs. Both carbon addition and oxygen depletion yielded similar results in this regard. Considering the fact that the carbon favors these longer chains so much in the outer disk, it is important to include them in chemical models. Pebble dynamics and ices being more oxygen dominated in the outer disk as described in Krijt et al. (2020) might explain why this C/O ratio exists in PDS-70.

Such a high C/O ratio has a significant effect on the $C^{18}O$ flux. Hence, in the future, the iterative method may need to be extended to include the C/O as a free parameter, so that results are consistent for both the $C^{18}O$ and C_2H line. Based on the results of this work, the expectation is that the C/O ratio of the gas will remain significantly larger than 1. Further study is also needed on whether a uniform C/O ratio will produce a good fit for the C_2H, or if it needs to be varied throughout the disk's radial extent, as the C_2H flux and abundance within 100 AU increases much faster with the C/O ratio than beyond this radius.

References

Aikawa, Y., Miyama, S. M., Nakano, T., and Umebayashi, T. (1996). Evolution of molecular abundance in gaseous disks around young stars: Depletion of co molecules. *The Astrophysical Journal*, 467:684.

Andrews, S. M. (2020). Observations of protoplanetary disk structures. *Annual Review of Astronomy and Astrophysics*, 58:483–528.

André, P. (2011). Spectral classification of embedded stars. *Encyclopedia of Astrobiology*, pages 1549–1553.

Benisty, M., Bae, J., Facchini, S., Keppler, M., Teague, R., Isella, A., Kurtovic, N. T., Pérez, L. M., Sierra, A., Andrews, S. M., Carpenter, J., Czekala, I., Dominik, C., Henning, T., Menard, F., Pinilla, P., and Zurlo, A. (2021). A circumplanetary disk around pds70c. *The Astrophysical Journal Letters*, 916:L2.

Brittain, S. D., Kamp, I., Meeus, G., Oudmaijer, R. D., and Waters, M. (2023). Herbig stars. *Space Science Reviews*, 219.

Cridland, A. J., Facchini, S., Dishoeck, v., and Benisty, M. (2023). Planet formation in the pds 70 system: Constraining the atmospheric chemistry of pds 70b and c. *arXiv (Cornell University)*.

Dubrulle, B., Morfill, G. E., and Sterzik, M. (1995). The dust subdisk in the protoplanetary nebula. *Icarus*, 114:237–246.

Eistrup, C., Walsh, C., and Dishoeck, v. (2018). Molecular abundances and c/o ratios in chemically evolving planet-forming disk midplanes. *Astronomy and Astrophysics*, 613:A14–A14.

Facchini, S., Teague, R., Bae, J., Benisty, M., Keppler, M., and Isella, A. (2021). The chemical inventory of the planet-hosting disk pds 70. *The Astronomical Journal*, 162:99.

Greenwood, A. J. (2018). *The Future of Protoplanetary Disk Models*. Rijksuniversiteit Groningen.

Henning, T. and Semenov, D. (2013). Chemistry in protoplanetary disks. *Chemical Reviews*, 113:9016–9042.

Isella, A., Benisty, M., Teague, R., Bae, J., Keppler, M., Facchini, S., and Pérez, L. (2019). Detection of continuum submillimeter emission associated with candidate protoplanets. *The Astrophysical Journal Letters*, 879:L25–L25.

Kamp, I., Thi, W.-F., Woitke, P., Rab, C., Bouma, S., and Ménard, F. (2017). Consistent dust and gas models for protoplanetary disks : Ii. chemical networks and rates. 607.

Keppler, M., Teague, R., Bae, J., Benisty, M., Henning, T., van Boekel, R., Chapillon, E., Pinilla, P., Williams, J. P., Bertrang, G. H.-M., Facchini, S., Flock, M., Ginski, C., Juhasz, A., Klahr, H., Liu, Y., Müller, A., Pérez, L. M., Pohl, A., Rosotti, G., Samland, M., and Semenov, D. (2019). Highly structured disk around the planet host pds 70 revealed by high-angular resolution observations with alma. *Astronomy Astrophysics*, 625:A118.

Krijt, S., Bosman, A. D., Zhang, K., Schwarz, K. R., Ciesla, F. J., and Bergin, E. A. (2020). Co depletion in protoplanetary disks: A unified picture combining physical sequestration and chemical processing. *The Astrophysical Journal*, 899:134–134.

Law, C. J., Benisty, M., Facchini, S., Teague, R., Bae, J., Isella, A., Kamp, I., Öberg, K. I., Portilla-Revelo, B., and Rampinelli, L. (2024). Mapping the vertical gas structure of the planet-hosting pds 70 disk. *The Astrophysical Journal*, 964:190–190.

Liu, B. and Ji, J. (2020). A tale of planet formation: from dust to planets. *Research in Astronomy and Astrophysics*, 20:164.

Mannings, V. and Sargent, A. (1997). A high-resolution study of gas and dust around young intermediate-mass stars : Evidence for circumstellar disks in herbig ae systems. *The Astrophysical Journal*, page 490 : 792.

McElroy, D., Walsh, C., Markwick, A. J., Cordiner, M. A., Smith, K., and Millar, T. J. (2013). The umist database for astrochemistry 2012. *Astronomy Astrophysics*, 550:A36.

McMullin, J., Waters, B., Schiebel, D., Young, W., and Golap, K. (2007). Casa architecture and applications. *ASP Conference Series*, 376.

Mesa, D., Keppler, M., Cantalloube, F., Rodet, L., Charnay, B., Gratton, R., Langlois, M., Boccaletti, A., Bonnefoy, M., Vigan, A., Flasseur, O., Bae, J., Benisty, M., Chauvin, G., de Boer, J., Desidera, S., Henning, T., Lagrange, A.-M., Meyer, M., Milli, J., Müller, A., Pairet, B., Zurlo, A., Antoniucci, S., Baudino, J. L., Sevilla, S. B., Cascone, E., Cheetham, A., Claudi, R., Delorme, P., D'Orazi, V., Feldt, M., Hagelberg, J., Janson, M., Kral, Q., Lagadec, E., Lazzoni, C., Ligi, R., Maire, A.-L., Martínez, P., Ménard, F., Meunier, N., Perrot, C., Petrus, S., Pinte, C., Rickman, E., Rochat, S., Rouan, D., Samland, M., Sauvage, J.-F., Schmidt, B., Udry, S., Weber, L., and Wildi, F. (2019). Vlt/sphere exploration of the young multiplanetary system pds70. *Astronomy and Astrophysics*, 632:A25–A25.

Miotello, A., Kamp, I., Birnstiel, T., Cleeves, L. I., and Kataoka, A. (2022). Setting the stage for planet formation: Measurements and implications of the fundamental disk properties.

Müller, A., Keppler, M., Henning, T., Samland, M., Chauvin, G., Beust, H., Maire, A.-L., Molaverdikhani, K., van Boekel, R., Benisty, M., Boccaletti, A., Bonnefoy, M., Cantalloube, F., Charnay, B., Baudino, J.-L., Gennaro, M., Long, Z. C., Cheetham, A., Desidera, S., Feldt, M., Fusco, T., Girard, J., Gratton, R., Hagelberg, J., Janson, M., Lagrange, A.-M., Langlois, M., Lazzoni, C., Ligi, R., Ménard, F., Mesa, D., Meyer, M., Mollière, P., Mordasini, C., Moulin, T., Pavlov, A., Pawellek, N., Quanz, S. P., Ramos, J., Rouan, D., Sissa, E., Stadler, E., Vigan, A., Wahhaj, Z., Weber, L., and Zurlo, A. (2018). Orbital and atmospheric characterization of the planet within the gap of the pds 70 transition disk. *Astronomy Astrophysics*, 617:L2.

Oberg, N., Kamp, I., Cazaux, S., Woitke, P., and Thi, W.-F. (2022). Circumplanetary disk ices. i. ice formation vs. viscous evolution and grain drift. *arXiv (Cornell University)*.

Pinte, C. (2015). Continuum radiative transfer. *EPJ Web of Conferences*, 102:00006.

Pinte, C., Harries, T. J., Min, M., Watson, A. M., Dullemond, C. P., Woitke, P., Ménard, F., and Durán-Rojas, M. C. (2009). Benchmark problems for continuum radiative transfer - high optical depths, anisotropic scattering, and polarisation. 498:967–980.

Portilla-Revelo, B., Kamp, I., Facchini, S., van Dishoeck, E. F., Law, C., Rab, C., Bae, J., Benisty, M., Öberg, K., and Teague, R. (2023). Constraining the gas distribution in the pds 70 disc as a method to assess the effect of planet-disc interactions. *Astronomy Astrophysics*, 677:A76.

Portilla-Revelo, B., Kamp, I., Rab, C., van Dishoeck, E. F., Keppler, M., Min, M., and Muro-Arena, G. A. (2021). Self-consistent modelling of the dust component in protoplanetary and circumplanetary disks: the case of pds 70. *Astronomy Astrophysics*, 658:A89.

Rampinelli, L., Facchini, S., Leemker, M., Bae, J., Benisty, M., Teague, R., Law, C. J., Öberg, K. I., Portilla-Revelo, B., and Cridland, A. J. (2024). Alma high-resolution observations unveil planet formation shaping molecular emission in the pds 70 disk. *Astronomy and Astrophysics*, 689:A65–A65.

Riaud, P., Mawet, D., Absil, O., Boccaletti, A., Baudoz, P., Herwats, E., and Surdej, J. (2006). Coronagraphic imaging of three weak-line t tauri stars: evidence of planetary formation around pds 70. *Astronomy and Astrophysics*, 458:317–325.

Sartori, M. J., Gregorio-Hetem, J., Rodrigues, C. O., Hetem, A., and Batalha, C. (2009). Analysis of the pico dos dias survey herbig ae/be candidates. 139:27–38.

Teague, R., Henning, T., Guilloteau, S., Bergin, E. A., Semenov, D., Dutrey, A., Flock, M., Gorti, U., and Birnstiel, T. (2018). Temperature, mass, and turbulence: A spatially resolved multiband non-lte analysis of cs in tw hya. *The Astrophysical Journal*, 864:133–133.

Visser, R., Bruderer, S., Cazzoletti, P., Facchini, S., Heays, A. N., and van Dishoeck, E. F. (2018). Nitrogen isotope fractionation in protoplanetary disks. *Astronomy Astrophysics*, 615:A75.

Williams, J. P. and Cieza, L. A. (2011). Protoplanetary disks and their evolution. *Annual Review of Astronomy and Astrophysics*, 49:67–117.

Woitke, P. (2015). Heating and cooling processes in disks. *EPJ Web of Conferences*, 102:00011–00011.

Woitke, P., Kamp, I., and Thi, W.-F. (2009). Radiation thermo-chemical models of protoplanetary disks i. hydrostatic disk structure and inner rim. *Astronomy and Astrophysics*, 501:383–406.

Woitke, P., Min, M., Pinte, C., Thi, W.-F., Kamp, I., Rab, C., Anthonioz, F., Antonellini, S., Baldovin-Saavedra, C., Carmona, A., Dominik, C., Dionatos, O., Greaves, J., Güdel, M., Ilee, J. D., Liebhart, A., Ménard, F., Rigon, L., Waters, M., Aresu, G., Meijerink, R., and Spaans, M. (2016). Consistent dust and gas models for protoplanetary disks. *Astronomy astrophysics*, 586:A103–A103.

Zhang, K., Booth, A. S., Law, C. J., Bosman, A. D., Schwarz, K. R., Bergin, E. A., Öberg, K. I., Andrews, S. M., Guzmán, V. V., Walsh, C., Qi, C., , v., Long, F., Wilner, D. J., Huang, J., Czekala, I., Ilee, J. D., Cataldi, G., Bergner, J. B., Aikawa, Y., Teague, R., Bae, J., Loomis, R. A., Calahan, J. K., Alarcón, F., Ménard, F., Gal, R. L., Sierra, A., Yamato, Y., Nomura, H., Tsukagoshi, T., Pérez, L. M., Trapman, L., Liu, Y., and Furuya, K. (2021). Molecules with alma at planet-forming scales (maps). v. co gas distributions. *The Astrophysical journal. Supplement series/Astrophysical journal. Supplement series*, 257:5–5.